Looped-Oxide Catalysis: A Solar Thermal Approach to Bio-Oil Deoxygenation

Journal:	*Energy & Environmental Science*
Manuscript ID:	EE-PER-05-2014-001684.R2
Article Type:	Perspective
Date Submitted by the Author:	30-May-2014
Complete List of Authors:	Hargus, Cory; Brown University, Michalsky, Ronald; Brown University, Peterson, Andrew; Brown University, School of Engineering

Looped-Oxide Catalysis: A Solar Thermal Approach to Bio-Oil Deoxygenation

Cory Hargus, Ronald Michalsky †, Andrew A. Peterson*

School of Engineering, Brown University, Providence, Rhode Island, 02912, United States.
† *Current address: Institute of Energy Technology, ETH Zurich, ML K 23 Sonneggstr. 3 CH-8092, Zurich, Switzerland.*
* *Corresponding author: Andrew_Peterson@brown.edu*

Abstract

A critical step in the conversion of pyrolysis and liquefaction bio-oils to transportation fuels is deoxygenative upgrading. With this perspective we introduce a two-step thermochemical cycle which harnesses concentrated solar radiation to drive bio-oil deoxygenation. In this cycle, which we have termed "looped-oxide catalysis" (LOC), a metal oxide is reduced in a high-temperature solar thermal reactor and subsequently reacted with bio-oil, reforming the original metal oxide and yielding a deoxygenated biofuel product. By augmenting the chemical energy stored in bio-oil with solar thermal energy, LOC may increase fuel yields for a given quantity of biomass beyond what is currently achievable with standalone biomass-to-fuel pathways. We identify five promising candidate LOC materials based on equilibrium thermodynamics, diffusion kinetics and catalytic performance in hydrodeoxygenation (HDO) reactions. Additionally, we present new experimental results and mechanistic implications from an investigation of the LOC upgrading of acetic acid. The formation of acetaldehyde with comparable selectivity in LOC with zinc metal as well as HDO with zinc oxide suggests that surface oxygen vacancies are the catalytically relevant sites in both processes.

Keywords: bio-oil, hydrodeoxygenation, solar thermal, chemical looping combustion, biomass conversion

1 Introduction

Instabilities in the price of petroleum and the impact of fossil fuel combustion on global climate change provide a demand for clean and renewable sources of transportation fuels, which ideally will not require major changes to the existing infrastructure for fuel consumption. Given the high energy density of liquid hydrocarbon fuels, it is likely that such fuels will continue to play a dominant role in the foreseeable future of the transportation industry. While petroleum derivatives constitute the bulk of transportation fuels currently in use, there are many available upgrade pathways for converting lignocellulosic biomass into value-added fuels including gasification followed by Fischer-Tropsch Synthesis (FTS) and hydroprocessing of pyrolysis and liquefaction bio-oils. Recent studies estimate the potential for lignocellulosic biomass production in the United States

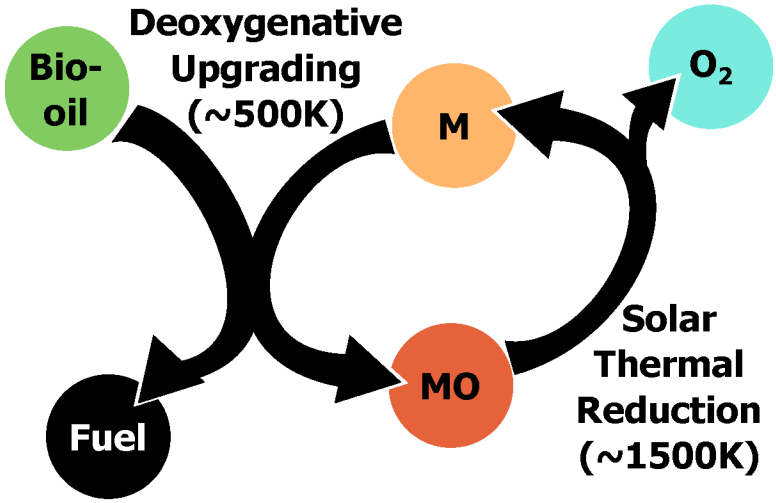

Figure 1: Overview of the looped-oxide catalysis (LOC) thermochemical cycle for bio-oil feed stock deoxygenation. MO denotes a metal oxide and M represents either the corresponding zero-valent metal or a lower-valence metal oxide.

through dedicated fuel crops as well as agricultural and municipal wastes at 1.3 billion dry tons per year with current technology and agricultural practices; enough to replace roughly one-third of the nation's current petroleum consumption [1–3]. Although this result is promising, the ultimate failure of biomass to meet one-hundred percent of liquid fuel needs illustrates a central problem of standalone biofuel production pathways which rely on biomass as the main source of energy. Namely, lignocellulosic biomass has a high oxygen content and, consequently, a relatively low combustion energy density. As a result, standalone biomass-to-fuels processes typically pay the energetic debt of deoxygenation by removing oxygen atoms as CO_2, for example, as a respiration product in microbial fermentation or a water-gas shift product in FTS.

The poor carbon-atom economy of standalone biofuel production processes has recently spurred the development of augmented pathways which utilize externally generated reducing agents — mainly H_2 — to drive the deoxygenation of biomass while achieving complete conversion of carbon atoms from biomass into fuels. For example, Dietenberger and Anderson have proposed incorporating sustainably-produced (*e.g.* nuclear or solar) H_2 into biomass gasification processes to remove oxygen as H_2O, arguing that a synergism between biomass synfuel and hydrogen production will be more cost-competitive than either fuel independently [4]. This analysis suggested a doubling or tripling of fuel output from a given quantity of biomass. In the analysis of Singh *et al.* [5] the fuel energy yield of biomass fast pyrolysis followed by hydroprocessing with solar H_2, on an arable-land basis, is estimated at 49.8 MJ m^{-2} $year^{-1}$. In comparison, the estimated yield of standalone biomass gasification followed by Fischer-Tropsch Synthesis is 20.9 - 25.5 MJ m^{-2} $year^{-1}$ and the yield of standalone biomass fermentation to ethanol is estimated at an even lower 18 - 25.2 MJ m^{-2} $year^{-1}$ [5]. These estimates indicate the potential for augmented biofuel production processes, which treat biomass as a material input while utilizing external sources of renewable energy to maximize fuel output, to generate up to a threefold increase in fuel yield over standalone processes for a given quantity of lignocellulosic biomass. If applied to the estimated 1.3 billion dry tons of available biomass, such augmented processes have the potential to enable complete replacement of petroleum-derived transportation fuels in the United States.

In this perspective, we present a new augmented biofuel production pathway which indirectly harnesses solar thermal energy to drive the deoxygenation of bio-oil. This process, which we have termed "looped-oxide catalysis" (LOC), is envisioned as a two-step thermochemical cycle, illustrated in Figure 1. In one step of the cycle, bio-oil is upgraded by reaction with a reduced metal oxide, forming a higher-valence oxide and yielding a deoxygenated fuel product. During this upgrading step, the reduced metal oxide provides both a bulk source of reducing potential to drive the deoxygenation reaction and a catalytic surface on which the reaction may proceed, thereby promoting both the thermodynamics and the kinetics of the reaction. "Catalysis" in this context is used specifically to refer to the role of the metal oxide surface chemistry in determining the rate of formation and yield of deoxygenation products within a wider range of possible reaction products. In the opposing step of the cycle, the metal oxide is heated in a solar furnace to the point at which it dissociates to its metal or to a lower-valence metal oxide and oxygen gas, thereby completing the cycle. Through the input of solar thermal energy, LOC has the potential to achieve significantly increased fuel yields over standalone biomass-to-fuels pathways, as has been discussed for related augmented biofuel production processes in the previous paragraph. We note that other processes can be envisioned to regenerate the reduced metal oxide, *e.g.*, involving very-high-temperature nuclear reactors, carbothermal reduction or electrochemical processing, but in the current work we focus on solar thermal regeneration due to the unambiguous renewable nature and the large body of research focused on that area.

We view this process as a complement and alternative to the hydroprocessing of bio-oil, which in most current applications is limited by requisite high H_2 pressures and by the destruction of chemical exergy during the reaction of H_2 with easily-reduced oxygenate compounds. Zero-valent metals including Fe, Zn and Al have previously been investigated with promising results for the reduction of many organic and inorganic carbon-containing compounds [6–11]. Recently, ceria-based redox cycles have also been implemented for the splitting of CO_2 to CO and O_2 [12–14], with peak solar-to-fuel energy conversion efficiencies above 3.5% [12]. Finally, the formation and subsequent hydrolysis of metal nitrides has been demonstrated in a solar thermochemical cycle as a means of producing ammonia at low pressures [15, 16]. It is the purpose of this perspective to examine the coupling of the solar thermal reduction of metal oxides to the direct deoxygenation of bio-oil, forming a complete thermochemical cycle, and to present a rational approach to catalyst selection and process design.

LOC incorporates concepts from the fields of catalytic hydroprocessing and solar thermochemical processing, and in Section 2 we will place LOC within the context of these technologies. In Section 3 we develop a rationale to select metal oxide redox cycles for application in LOC based on bulk thermodynamics, as well as a consideration of diffusion kinetics and surface catalytic activity and other properties. In Section 4 we present and discuss experimental results of this concept as well as their mechanistic implications. To do this, we employ a continuous flow LOC reaction of zinc metal with acetic acid, which is used as a simple model compound for bio-oil. Finally, in Section 5 we outline the relative merits of LOC *vs.* catalytic hydroprocessing as well as the challenges that remain for developing LOC as a technology.

Table 1: Characteristics of bio-oils and heavy fuel oil. Adapted [a]from Elliott [23] and [b]from Czernik [24]

Physical property	Liquefaction bio-oil[a]	Flash pyrolysis bio-oils[a]	Heavy fuel oil[b]	HDO-upgraded bio-oil[a]
Moisture (wt%)	5	25	0.1	.001-.008
Elemental analysis (*dry basis wt%*)				
C	73	44	85	85-89
H	8	7	11	11-14
O	16	49	1	0.0-0.7
HHV (MJ/kg)	35.7	22.6	40.0	42.3-45.4
Viscosity (cPs)	15,000 at 61 °C	59 at 40 °C	180 at 50 °C	1.0-4.6 at 23 °C

2 Background Technologies

The design of looped-oxide catalysis (LOC) processes draws on the large body of knowledge surrounding catalytic hydroprocessing and solar thermal hydrogen production technology, both of which will be discussed in this section. As a result, LOC can benefit directly from independent and ongoing research in each of these distinct fields.

2.1 Catalytic Hydroprocessing

Bio-oils obtained from the thermal processing of lignocellulosic biomass represent a promising feedstock for the production of renewable fuels; however, without deep deoxygenative upgrading their direct use as a fuel is severely limited. One route for bio-oil deoxygenation that has been extensively investigated is catalytic hydroprocessing, a technology adapted from the hydroprocessing of petroleum fuels. In general, hydroprocessing involves the addition of hydrogen gas into a low-grade liquid fuel in the presence of a solid catalyst. The goal of hydroprocessing is to improve fuel quality by removal of heteroatoms, resulting in higher energy content, volatility and thermal stability and lower viscosity and molecular weight [17, 18]. Because oxygen is the predominant heteroatom in bio-oil (see Table 1), studies of bio-oil hydroprocessing tend to focus on hydrodeoxygenation (HDO) as the primary reaction pathway. To maximize efficiency and minimize the amount of H_2 consumed during upgrading, a successful HDO catalyst should selectively reduce carbon-oxygen bonds while leaving carbon-carbon double bonds unsaturated. Additionally, catalysts should minimize deactivation through poisoning by sulfur and nitrogen compounds and through coke deposition [19–22].

There are two principal avenues leading from raw lignocellulosic biomass to bio-oils: fast pyrolysis and liquefaction. Fast pyrolysis is the rapid thermal decomposition of biomass in the absence of oxygen, and is characterized by moderate temperatures (around 500°C) and short residence times (normally less than two seconds) [25, 26]. Liquefaction, on the other hand, is the decomposition of biomass under hydrothermal conditions, characterized by lower temperatures (200 to 370°C) and high pressures (4 to 20 MPa) [18]. Due to their high oxygen contents, both fast pyrolysis and liquefaction oils are generally unusable without deep upgrading, which can be accomplished with

catalytic hydroprocessing. The removal of oxygen heteroatoms from bio-oils during hydroprocessing occurs by decarboxylation, thermal cracking and, predominantly, hydrodeoxygenation (HDO). For bio-oil with an overall empirical formula of $C_6H_9O_4$, these reactions can respectively be considered as: [4, 27].

$$C_6H_9O_4 \longrightarrow C_4H_9 + 2\,CO_2 \tag{1}$$

$$C_6H_9O_4 \longrightarrow C_{4.5}H_7 + H_2O + 1.5\,CO_2 \tag{2}$$

$$C_6H_9O_4 + 4\,H_2 \longrightarrow C_6H_9 + 4\,H_2O \tag{3}$$

Early investigations into bio-oil hydroprocessing during the 1980s and 1990s utilized the same sulfided CoMo and NiMo catalysts that have been successful in petrochemical upgrading processes, where hydrodesulfurization (HDS) and hydrodenitrogenation (HDN) are the primary reaction pathways [25]. Research continues on the use of sulfided catalysts for hydroprocessing of bio-oils [28, 29]. It is important to note, however, that many sulfided and aluminosilicate HDS catalysts were developed to operate in non-aqueous environments, and can be unstable in the high-moisture-content conditions typical of bio-oil. Furthermore, deoxygenative upgrading of bio-oil seeks to reduce the oxygen content from up to 50% to an acceptable level below 1%, while the objective of HDS catalysts is to achieve deep desulfurization, generally to around 15 ppm [30] As a consequence, more recent research efforts have sought to explore new classes of catalysts, particularly non-sulfided CoMo and NiMo on titania and zirconia supports and supported late transition metals [7, 17, 25, 28, 31–33]. Attention has also recently turned to metal oxide catalysts capable of forming surface vacancies under reducing conditions. These catalysts, such as MoO_3, are believed to bind oxygen in bio-oil molecules at surface oxygen vacancy sites in a Mars-van Krevelen mechanism [34–36]. A similar mechanism is thought to be responsible for supported Mo, NiMo and CoMo catalysts in their sulfide and oxide forms [37].

2.2 Solar Thermochemical Generation of Hydrogen

The efficient production of H_2 from water via thermochemical cycles (TCs) is a longstanding goal of solar thermal research. The single-step thermal dissociation of water, although conceptually simple, has proven to be difficult to achieve due to the requirement of a high-temperature separation of the formed H_2 and O_2 [38–40]. TCs built around metal oxide redox cycling avoid this problem by generating H_2 and O_2 in separate steps in a process similar to chemical looping combustion. Such water-splitting cycles are composed of a high-temperature (generally $T \geq 1500$ K) endothermic metal oxide reduction step and a lower-temperature (400 K $< T <$ 700 K) exothermic re-oxidation step, given below.

$$MO_x \longrightarrow MO_{x-\delta} + \frac{\delta}{2}O_2 \tag{4}$$

$$MO_{x-\delta} + \delta H_2O \longrightarrow MO_x + \delta H_2 \tag{5}$$

Some of the metal oxide TCs under investigation include the redox pairs ZnO/Zn, MgO/Mg, Fe_3O_4/FeO, Mn_3O_4/MnO, Nb_2O_5/NbO_2, In_2O_3/In, SnO_2/SnO, CeO_2/Ce_2O_3 and others [9, 41–51]. Early research efforts in metal-oxide thermochemical cycling sought to utilize process heat from nuclear fission reactors, but because such heat sources generally operate below about 1200 K, the

number of possible cycles was very limited [52, 53]. More recently, the development of large-scale optical systems for concentrating solar radiation have opened the door to solar TCs capable of operating at much higher temperatures, even exceeding 2000 K [54]. For many metal oxides, however, the temperatures required for thermal dissociation are still too high for commercially-available reactor materials. To achieve reduction at lower temperatures, work must be added to the system in an amount equal to the ΔG_{rxn} at that temperature. This can be accomplished by holding the oxide at a negative potential in an electrolytic cell (electrothermal reduction), adding a chemical reducing agent such as carbon (carbothermal reduction), maintaining a sub-atmospheric pressure within the reactor (vacuum reduction), or any combination of these three.

Solar electrothermal reduction, in which the metal oxide is dissolved in a molten electrolyte supplied with solar heat and reduced in an electrolytic cell, was recently demonstrated by Krenzke *et al.* [55] for the reduction of ZnO to Zn in a 10 $\mathrm{kW_e}$ reactor at 1350 K and a current density of 0.5 A $\mathrm{cm^{-2}}$ with 47% of the energy of reduction provided by solar heat and the remainder supplied by electricity. Solar electrothermal reduction has been investigated for metal oxides including Al_2O_3, MgO and ZnO [43, 44, 56–60] and will be the focus of the analysis presented in this perspective.

3 Criteria for Successful LOC Cycles

The successful performance of any looped-oxide catalysis (LOC) thermochemical cycle is predicated on the fulfillment of at least three criteria. (1) The thermodynamics of the cycle must permit the deoxygenation of bio-oil oxygenates at the temperature of the upgrading reaction while minimizing the energetic cost of the high-temperature thermal or electrothermal reduction step. (2) Each reaction step must proceed at an acceptable rate, notably including the diffusion of oxygen through the higher-valence oxide surface during the upgrading reaction. (3) The higher-valence metal oxide surface formed during the upgrading step must function as a catalyst for the LOC deoxygenative upgrading reaction, where successful performance in HDO reactions is seen as an indicator of potential activity in LOC. Of course, many other factors will prove important in addition to these three constraints, such as susceptibility to catalyst poisoning, the cost and nature of any separation steps, the weight, toxicity and global availability of the candidate LOC oxide material, as well as the overall process economics in the volatile energy sector. Herein, we evaluate several candidate TCs based on these criteria.

Thermochemical optimization. Because the ultimate objective of LOC is the deoxygenation of bio-oil oxygenate compounds, the thermodynamic performance of this process in conjunction with the thermal reduction of a metal oxide is considered the primary criterion in candidate LOC cycle selection. In developing an effective metric for optimizing the selection of LOC materials we turn to an analogue in catalysis: the Sabatier Principle states that the interaction between a catalyst and its substrate should be neither too strong (the substrate will not desorb, blocking catalytic sites) nor too weak (the substrate will not adsorb and no reaction will occur) [61]. This simple concept is often invoked in catalyst engineering to create a "volcano plot" where the activities of different catalysts are plotted against the substrate binding energy or any other parameter pertaining to the catalyst's ability to form bonds with the substrate [62]. The Sabatier Principle may also be applied to looped-oxide catalysis: the reduced oxide should have an oxygen affinity that is sufficiently

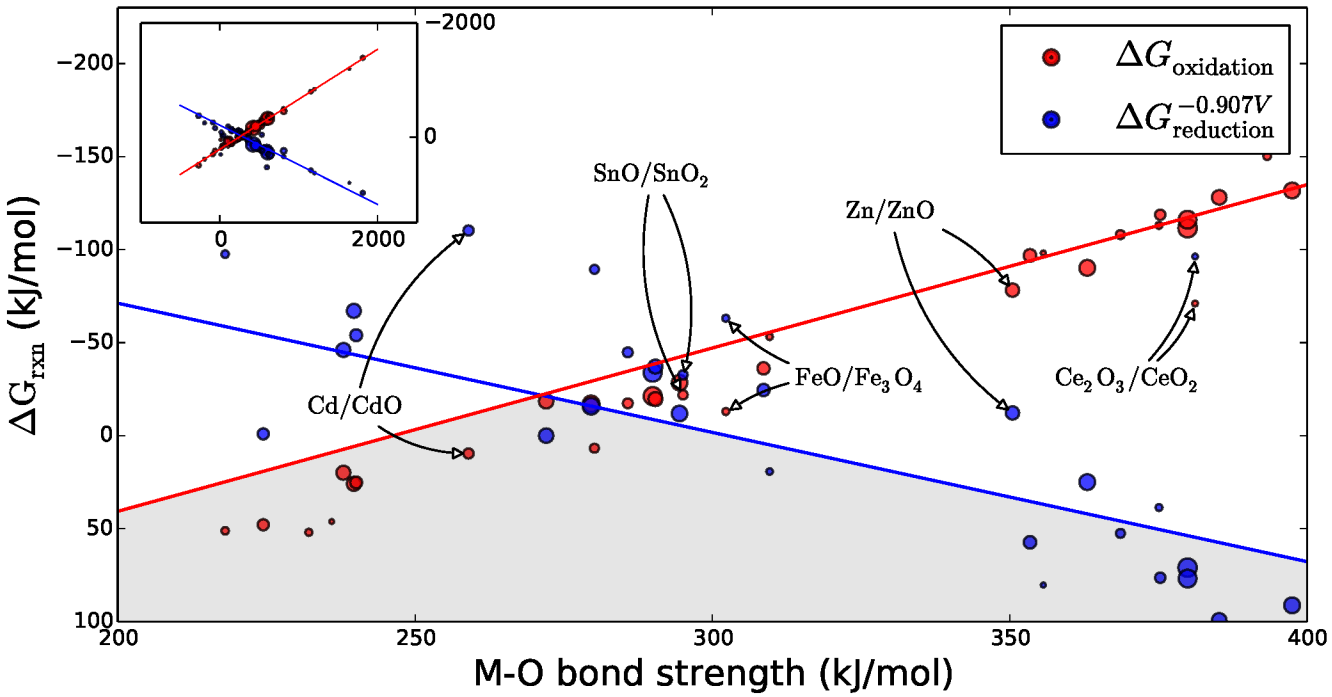

Figure 2: Volcano-type plot of LOC cycles, with the five candidate cycles annotated. Red and blue points represent, respectively, the ΔG of the reduced oxide reaction with acetic acid at 500 K in kJ/mole acetic acid (Equation 6) and ΔG of the solar thermal reduction at 1500 K and -.907 V in kJ/$\frac{1}{2}$ mole O_2 (Equation 4), plotted against ΔH of reduction at 500 K in kJ/$\frac{1}{2}$ mole O_2, which is used as a measure of the metal-oxygen bond strength. The inset figure depicts the volcano-type plot over its entire range of the 80 cycles included in this analysis. The red and blue functions are linear regressions for the plotted data points. The weight of each data point corresponds to the mass of oxide per mole of acetaldehyde generated; a larger dot indicates a greater yield of acetaldehyde per mass of oxide. The full data set is available in the supplementary information.

high to abstract oxygen atoms from the bio-oil oxygenate species, but also sufficiently low that the higher-valence oxide may be reduced in the solar furnace with a minimum input of heat and work.

With this idea in mind, we have utilized thermochemical data from the Barin and JANAF tables [63, 64] to identify desirable looped-oxide materials; that is, thermodynamically feasible pairs of metal oxides and their reduction products (either lower-valence oxides or zero-valent metals). Bio-oil contains a diverse range of oxygenate compounds, all of which may undergo deoxygenation through numerous reaction pathways. To make the analysis of looped-oxide catalysis (LOC) tractable, we have chosen acetic acid, CH_3COOH, as a model bio-oil oxygenate compound. The suitability of this compound as a simple model will be discussed further in Section 4. The LOC reduction of acetic acid to acetaldehyde, as represented in the reaction below, is therefore utilized as a model reaction for bio-oil deoxygenation.

$$MO_{x-\delta} + \delta CH_3COOH \longrightarrow MO_x + \delta CH_3CHO \tag{6}$$

In Figure 2, the Gibbs free energy of thermal reduction and the Gibbs free energy of re-oxidation by reaction with acetic acid is plotted for eighty LOC cycles against the corresponding enthalpy

of reduction, which is used as a metric of oxygen binding strength. The numeric values of thermodynamic quantities and reaction stoichiometries are provided in Appendix C of the Supporting Information. While the entire volcano is shown in the inset, the main figure highlights a detail of the volcano "peak" where the most thermodynamically-desirable metal oxide redox cycles exist, *i.e.* those with intermediate metal-oxygen bond strength. In this proxy analysis, it is assumed that the oxidation step takes place at 500 K and 1 bar and that the regeneration step takes place at 1500 K, 1 bar, and at a reduction potential of -.907 V. This is the potential necessary to make the reduction of FeO to Fe exergonic at 1500 K. This was chosen as a benchmark potential because the FeO/Fe cycle has the lowest enthalpy of reduction of all LOC cycles which achieve exergonic deoxygenation acetic acid at 500 K. It is also assumed that all oxides step sequentially through oxidation states during redox reactions and that discrete oxidation states exist for all oxides according to the stoichiometric values in the source of thermochemical data [63, 64].

The thermochemical analysis identifies a number of appealing LOC cycles, many of which are the same cycles that have demonstrated success in solar thermochemical water-splitting. We highlight a few interesting materials herein — FeO/Fe_3O_4, Zn/ZnO, Cd/CdO, SnO/SnO_2 and Ce_2O_3/CeO_2 — and discuss these materials in the context of their oxygen diffusion kinetics and performance as hydrodeoxygenation (HDO) catalysts.[1]

- **FeO/Fe_3O_4.** The use of metal-oxide thermochemical cycling for splitting water to produce hydrogen was first proposed for the redox pair FeO/Fe_3O_4 [38, 65]. To date this remains one of the most thoroughly studied systems in thermochemical cycling. Beyond its desirable thermodynamics, the principal advantages of iron oxide systems are low cost and high availability of materials [66]. Another notable feature of iron oxide systems is the potential for partial substitution in FeO/Fe_3O_4 by distinct metal oxides of the form MO/M_3O_4 to achieve more desirable thermochemical, kinetic and material properties in the formed ferrite material. Ferrites such as $Ni_{0.5}Mn_{0.5}Fe_2O_4$ [67] and $CuFe_2O_4$ [68] have been studied in thermochemical cycling applications both in the partially-substituted spinel crystal phase [69] and in ferrites synthesized through atomic layer deposition of alternating layers of, *e.g.*, Fe_2O_3 and CoO to achieve a bulk layered cobalt ferrite, $CoFe_2O_4$ [53]. The limiting factor in the kinetics will likely be due to the rate of diffusion of oxygen into the bulk of the metal [70, 71]. Also within the solar thermochemical community, recovery of process heat has proven difficult as quenching has been employed to avoid recombination of FeO with O_2 upon reduction. The rapid quenching to non-stoichiometric and nearly-stoichiometric wüstite, *e.g.* $FeO_{0.982}$, is often desirable as the oxidation of these phases by water is much more rapid than that of stoichiometric FeO due to the high presence of bulk defects [72]. Iron oxide has demonstrated catalytic ability in HDO; interestingly, its highest selectivity (up to 80%) in the vapor-phase hydrodeoxygenation of acetic acid to acetaldehyde was reported when iron is present in both its oxide and metallic phases [73, 74], as may be expected in some stages of an LOC process.

- **Zn/ZnO.** An intriguing cycle for LOC upgrading of bio-oil is Zn/ZnO. This cycle can exhibit very high exergy efficiency due to the relatively low heat capacity of ZnO, while achieving

[1] Figure 2 shows six exergonic reaction cycles with a metal-oxygen bond strength intermediate between the Cd/CdO and SnO/SnO_2 pairs, *i.e.*, in order of increasing metal-oxygen bond strength, Fe/FeO, Fe/Fe_3O_4, Sn/SnO, Ge/GeO_2, Sn/SnO_2 and Mo/MoO_2. While the zero-valent metals allow for an exergonic deoxygenation [10], reducing the metal oxides may be limited kinetically due to diffusion of oxygen through a solid metallic phase (Fe and Mo) or complicated due to mixing of liquid metal with the electrolyte (Sn and Ge).

high stoichiometric deoxygenation per mass of Zn. The thermal dissociation of ZnO to Zn was recently demonstrated with success in a 100 kW_{th} pilot plant which yielded condensed products with a Zn molar fraction of up to 49% [75]. As with the FeO/Fe_3O_4 cycle, the rate of diffusion of oxygen interstitials and vacancies through ZnO may be expected to limit the kinetics; however, a means of achieving high (>50%) oxidation yields has been to employ Zn nanoparticles (diameter <100 nm), which may be synthesized from Zn vapor in the regeneration step [42]. Indeed, care must be taken in the cooling of the Zn vapor to achieve good Zn metal recovery and avoid recombination with oxygen [53]. In practice, regulation of quenching parameters following the regeneration step allows for good control over material properties including particle size of the Zn metal, which will affect both its internal mass transfer limitations as well as its catalytically active surface area. Another approach to regeneration is to conduct the reduction of ZnO in a thermal electrolytic cell at above the boiling point of Zn; this results in the evolution of gaseous Zn metal at the cathode and oxygen at the anode, a simple separation step that allows for greater flexibility in the Zn metal quenching conditions without recombination of products upon cooling [60]. Reduction of ZnO by "quasi-electrolysis" has also been suggested, wherein a supersaturated solution of ZnO is heated in an electrolytic cell to a temperature at which reduction is exergonic but maintained at high-pressure to suppress spontaneous dissociation [58]. Low-voltage electrolysis of the solution then evolves gaseous Zn and O_2 at separate electrodes and the electrical energy supplied simply becomes the energy of unmixing of gaseous Zn and O_2, about 19 kJ [56]. Catalytically, ZnO exhibited activity towards the selective deoxygenation of acetic acid to acetaldehyde with a peak selectivity of 20% occurring at 338°C. ZnO has also demonstrated activity towards hydrogenation of aromatic carboxylic acids. In particular, ZnO has been shown to catalyze the hydrodeoxygenation of benzoic acid to benzaldehyde with high yields of around 90% at 350°C, and with additional deoxygenation to toluene occurring at 380°C [76].

- **Cd/CdO.** Of the five candidate oxides examined in this section, cadmium oxide exhibits the lowest thermodynamic barrier to reduction. As with zinc oxide, the Cd/CdO cycle requires a quenching step after reduction. Although recombination with oxygen during the quenching process may lead to a loss in cadmium metal recovery, an electrolytic set-up may be utilized to achieve separation. It may also be possible to bypass diffusion limitations inherent to other metal oxide TCs by carrying out the re-oxidation of cadmium in its molten liquid state [77]. The toxicity of cadmium, however, limits its prospects for fuel upgrading and also dictates the role of process byproducts such as waste mineral ash [78]. To our knowledge cadmium oxide has not been investigated as a catalyst for bio-oil deoxygenation; however, previous research has demonstrated the activity of CdO as a Lewis-acid catalyst for the hydrolysis, esterification and transesterification of triglycerides and fatty acids in bio-diesel production [79].

- **SnO/SnO_2.** SnO is metastable at temperatures above 600 K and will disproportionate into Sn and SnO_2 [80]. As with the non-stoichiometric wüstite phases in the iron oxide cycle, fast oxidation kinetics have been observed for the hydrolysis of SnO with no passivation effect occurring in the formed oxide surface layer. However, the oxidation kinetics of a mixture of Sn and SnO_2 have been demonstrated to be slower, requiring approximately one hour of reaction time to achieve 70% conversion of micron-sized particles at 525°C [47]; therefore it may be preferable to suppress disproportionation as much as possible. For this reason we

have based the analysis in this perspective on the formation of SnO as the reduction product. Hydroprocessing of bio-oils over SnO_2 catalysts has been proposed [81] and demonstrated for the HDO of acetic acid with relatively high selectivity (40%) occurring at a temperature of 450°C [82]. A higher selectivity of 75% was achieved when SnO2 was used as a support for platinum prepared by wet impregnation. The higher activity is attributed to the ability of platinum and other late transition metal to activate hydrogen, which may then react with acetic acid at the metal-support interface.

- **Ce_2O_3/CeO_2.** Thermochemical cycles utilizing pure or doped ceria have recently demonstrated great promise for both water-spliting and CO_2 reduction applications due to the high rate of oxygen vacancy migration in these materials [12–14,83]. Fast vacancy diffusion kinetics have also made doped ceria an attractive material for solid oxide fuel cells [84]. In solar thermochemical water-splitting, 100% conversion of mm-sized Ce_2O_3 particles to CeO_2 was observed in less than five minutes at 600°C [85]. Thermochemical cycles involving ceria are often discussed in terms of intermediate, non-stoichiometric oxidation states, where a redox cycle has the form $CeO_{2-\delta}$/CeO_2 [86]. Values of oxygen deficiency, δ, were found to range between 0.016 and 0.042 in reticulated porous ceria after solar theral reduction at temperatures from 1400 to 1600°C [12]. Without achieving higher oxygen deficiency, this cycle's primary limitation is the relatively low stoichiometric yield of upgraded bio-oil per mass of ceria. Catalytically, CeO_2 has exhibited high selectivity in the vapor-phase hydrodeoxygenation of benzoic acid to benzaldehyde at temperatures below 350°C. At temperatures above 375°C, near-complete conversion of benzoic acid was accompanied by increased formation of the more deoxygenated product toluene [87].

Efficiency comparison of LOC and HDO. Although detailed process engineering and economic analyses are beyond the scope of this perspective, an exergy analysis of the looped-oxide catalytic upgrading of acetic acid to acetaldehyde such as the one presented in Appendix B can provide insight into the thermodynamic bottlenecks of the process as well as an assessment of the best-case performance of LOC. Typical efficiency values for the five candidate LOC materials described above in an LOC process incorporating solar electrothermal reduction range from 25 to 43%, assuming no heat recovery during the quenching of solar thermal reduction products. This analysis assumes perfect optics and insulation, absorptivity and emissivity approaching unity, solar influx of 1 kW/m^2 and further assumes electricity for driving the electrothermal reduction is available from ideal p-n junction solar photovoltaic (PV) cells operating at the Shockley-Queisser limiting efficiency of 33.7%. The PV cell area required for the electrothermal LOC upgrading of 1 mole of acetic acid to acetaldehyde per second at ambient pressure ranges from 180 to 530 m^2 with the combined heliostat and PV areas ranging from 570 to 930 m^2 (see Appendix B, Supporting Information).

In comparison to LOC, the efficiency of any hydrodeoxygenation (HDO) process is categorically limited by the generation and compression of H_2. A best-case efficiency for HDO of acetic acid to acetaldehyde with H_2 produced from solar photovoltaic water-splitting is roughly 30% if operated at 100 bar. This assumes hydrogen is produced from the electrolysis of water with 100% efficiency, where electricity is supplied from ideal p-n junction solar PV collection with the Shockley-Queisser limiting efficiency of 33.7%, as well as assuming complete conversion and ideal isothermal compression of H_2 from 1 to 100 bar. The total PV cell area required for HDO of acetic

acid to acetaldehyde at a rate of 1 mole per second with H_2 produced from solar electrolysis is 740 m^2.

The combined heliostat and PV cell areas required for the electrothermal LOC upgrading of acetic acid to acetaldehyde are in all cases below 1000 m^2. To put these numbers in perspective: assuming a biomass growth rate of 3 kg $\mathrm{m}^{-2}\,\mathrm{year}^{-1}$ (a typical value for the feed crop *Miscanthus* [88]) and representing the biomass with a stoichiometrically-equivalent amount of acetic acid in the model system, the cultivation of a sufficient amount of biomass to sustain the flow rate assigned in our calculations would require 130,000 m^2 of arable land. This area is two orders of magnitude greater than the area required for heliostat and photovoltaic solar collection. This result illustrates how, by dedicating a relatively small portion of arable land (less than 1% of the total land area) to solar thermal and PV collection and coupling this process to the upgrading of biomass from the remainder of the land area, it may be possible to significantly increase the total fuel yield.

4 Experimental Investigation of LOC Upgrading Reaction

In this section, we present new experimental results of an LOC upgrading reaction of zinc metal with acetic acid, which is used as a model feedstock compound for bio-oil. Lower carboxylic acids are a common component of bio-oils, constituting 5-10 wt% of a typical bio-oil sample [89]. The deoxygenation of carboxylic acids is also a useful benchmark reaction because the high acidity of bio-oils (pH of 2-3) renders bio-oils unstable and corrosive [90–92]. Finally, the hydrodeoxygenation (HDO) of acetic acid to acetaldehyde is well-characterized over a wide range of metal oxide catalysts [82, 93–95]. Clearly, further studies will be needed on LOC deoxygenation with actual pyrolysis and liquefaction bio-oil and many other model compounds for this process to be developed; herein we choose acetic acid only for its ability to provide us with unambiguous evidence of reaction mechanisms and to make direct comparisons to standard HDO experiments with the same compound. Of the five candidate cycles identified in the previous section, the Zn/ZnO cycle was chosen as an interesting starting point for an LOC demonstration. This cycle is considered to be one of the most promising metal oxide redox cycles for thermochemical water-splitting, given its high exergy efficiency and relatively low dissociation temperature (2320 K) [41, 75, 96]. Additionally, ZnO has demonstrated activity towards hydrodeoxygenation in previous studies [82, 93, 97]. We have also investigated the analogous case of acetic acid hydrodeoxygenation (HDO) with a zinc oxide catalyst and will discuss the relationship between the results of these two experiments, showing that the LOC experiments can give insight on the reaction mechanisms in the HDO experiments.

4.1 Methods

The LOC upgrading of acetic acid (Fisher, 99.9%) was performed in a continuous flow reactor setup (Figure 3). This setup consisted of a stainless steel 316 pre-heating coil (0.25 in. o.d., 0.02 in. wall thickness and 40 in. length) fitted to a stainless steel 316 fixed-bed reactor. Both the pre-heating coil and reactor were submerged in a heated sand bath, and temperature was monitored throughout the flow setup. An argon (PurityPlus, UHP Grade, 99.999%) gas stream with a volumetric flow rate of 45 cm^3(STP)min^{-1} was sparged through acetic acid at 20°C and 1.1 bar, achieving a saturation vapor pressure of 21 mbar. The saturated argon carrier gas was then passed through a fixed-bed reactor held at 350°C and containing 125 mmol (8.2 g) zinc metal powder (Noah Tech, 99.9%,

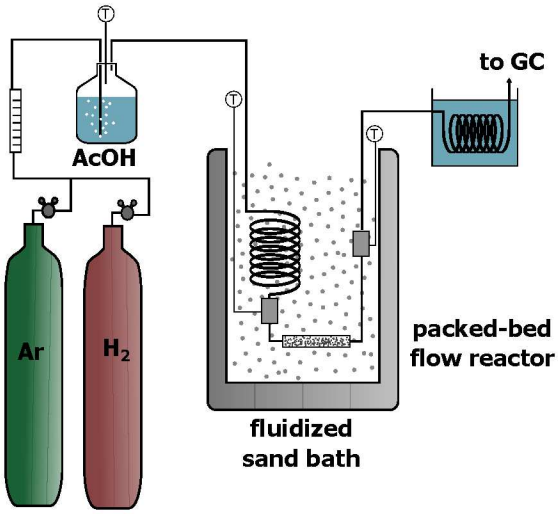

Figure 3: Process flow diagram of the experimental setup for the HDO and LOC upgrading of acetic acid.

<5 μm avg.) packed with deactivated borosilicate glass wool. The product stream was cooled and monitored quasi-continuously with an on-line gas chromatograph (Agilent 7890A) equipped with an HP-PLOT/U capillary column, flame ionization detector and thermal conductivity detector. Methane, ethylene, ethane, acetylene, propylene, propane, acetaldehyde, ethanol, acetone, ethyl acetate, acetic acid, CO_2 and CO were monitored simultaneously as potential reaction products. Because of the low vapor pressure of acetic acid relative to the reaction products, all species in the product stream remained in the vapor phase and no condensate was observed.

In the analogous HDO investigation the same experimental setup and flow parameters were used but H_2 (PurityPlus, UHP Grade, 99.999%) replaced argon as the carrier gas and ZnO (Noah Tech, 99.999%, <5 microns avg.) was used as the catalyst, with a reactor loading of 125 mmol (10.2 g). In the HDO experiment, the temperature of the reactor was increased from 300°C to 425°C at a rate of 1°C/min with samples taken every 25 minutes. In both the HDO and LOC experiments, the catalyst surface was pretreated in H_2 flow of 20 cm^3(STP)min^{-1} for one hour at 300°C. A carbon-weighted selectivity was calculated for the organic products using the following formula:

$$\text{Selectivity}_i(\%) = \frac{p_i C_i}{\sum_i p_i C_i} \tag{7}$$

Here p_i refers to the partial pressure of a given product, i, as determined by gas chromatography and C_i refers to the number of carbon atoms in each product species.

4.2 Results and Discussion

HDO. As a control experiment, we first carried out HDO of acetic acid on ZnO to facilitate validation with the literature. The selectivity toward acetic acid and dominant organic products during the ZnO-catalyzed HDO reaction is plotted in Figure 4. These results are consistent with the literature for carboxylic acid HDO over a metal oxide catalyst [30, 73, 82]. The primary byproduct of the reaction is acetone, which is produced at all temperatures via the ketonization reaction:

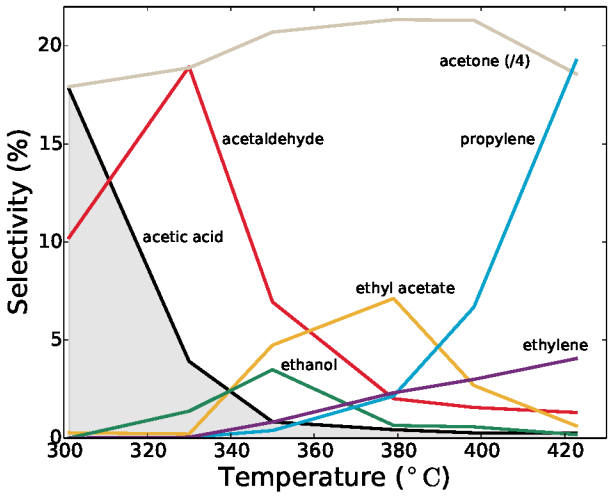

Figure 4: HDO control experiment. Plotted is the carbon-weighted selectivity (see Equation 7) as a function of temperature for acetic acid and the dominant organic products of ZnO-catalyzed HDO. The acetone selectivity values have been divided by four for ease of reading.

$$2\,CH_3COOH \longrightarrow CH_3COCH_3 + CO_2 + H_2O \tag{8}$$

The net conversion of acetic acid to products is greater at higher temperatures. Peak selectivity to the deoxygenation product, acetaldehyde, was observed at 19% at a temperature of 325°C. This is in good agreement with the results of a previous study by Pestman *et al.* which also utilized ZnO as a catalyst for acetic acid hydrodeoxygenation, obtaining a peak selectivity to acetaldehyde of 20% at a temperature of 338°C [82]. The formation of ethanol is also observed at intermediate temperatures along with ethyl acetate, which has been suggested to be formed via the Fischer esterification reaction and/or the Tishchenko reaction [93, 95]. Finally, formation of the more-fully hydrodeoxygenated products propylene and ethylene is seen to be favored at temperatures exceeding 380°C.

LOC. Next, we used a reduced Zn catalyst in an argon environment with the same acetic acid reagent, in order to assess the LOC reaction (in a H_2-free environment). In Figure 5 the selectivity toward dominant products of the 350°C LOC experiment is plotted as a function of total reaction time, where the dotted lines give the corresponding product selectivity observed in the HDO experiment at 350°C. This reaction can be decomposed into two general temporal regimes. In the first regime, which lasts for the first sixty minutes of the reaction, the conversion of acetic acid to products is nearly complete. The selectivity to acetaldehyde is observed to be 9.5%, slightly higher than in the corresponding HDO experiment at 350°C, and a small amount of ethyl acetate formation is also observed. In the second regime, which spans the remainder of the reaction, selectivity towards acetaldehyde undergoes decay, accompanied by an increase in unreacted acetic acid. This trend likely corresponds to a diffusion-limited regime, in which a passivating zinc oxide layer has formed on the surface of the zinc particles, such that any coordinatively unsaturated surface sites at which acetic acid deoxygenation may occur necessarily derive from diffusion of oxygen vacancies through this oxide layer towards the surface.

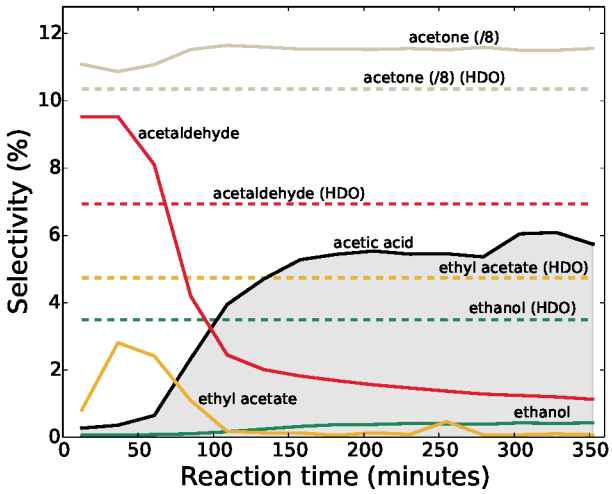

Figure 5: LOC experiment. Plotted is the carbon-weighted selectivity as a function of reaction time for acetic acid and the dominant organic products of LOC with Zn catalyst. The acetone selectivity values have been divided by eight for ease of reading

In the selection and design of more effective LOC materials, one of the primary goals will be to extend the first regime of high selectivity towards deoxygenation. This might be accomplished by utilizing materials with faster diffusion characteristics as well as using nano-sized catalyst particles. As discussed earlier, zinc is known to form a passivating oxide layer with relatively slow diffusion kinetics as observed during the water-splitting step of solar thermochemical hydrogen production [41, 42, 68, 75, 96]. Another objective in the design of LOC materials will be to achieve high selectivity towards deoxygenation without unwanted side reactions like the ketonization reaction of acetic acid to form acetone, as is known to occur on ZnO. It is worth noting that this was the dominant side reaction in both the LOC results and the HDO experiments reported here and in the literature [73, 82]

These results can also help us to understand the mechanisms in the HDO reaction. First, as discussed in more detail in the next section, the similar selectivities of LOC to HDO, when LOC only has oxygen vacancies as a reductive source, suggests that a Mars-van Krevelen-type reaction is responsible for deoxygenation in both cases. Second, the observation that a decrease in ethyl acetate formation after 100 minutes coincides with decreased acetaldehyde formation supports the hypothesis that ethyl acetate is formed via the Tishchenko reaction:

$$2\,CH_3CHO \longrightarrow CH_3COOCH_2CH_3 \tag{9}$$

Finally, it is important to note that a key objective of HDO catalysis is to achieve activity towards deoxygenation without expending H_2 on hydrogenation reactions that have relatively small energetic payoff (*e.g.* saturation of aromatic rings) [17]. By design, LOC achieves deoxygenation without hydrogenation by using a zero-valent metal or low-valence metal oxide as the reducing agent rather than H_2. This is demonstrated in Figure 5, where it can be seen that LOC achieves selectivity towards the deoxygenation product, acetaldehyde, while selectivity towards the hydrogenation product, ethanol, is suppressed, since H_2 is not available for the hydrogenation. (For additional yield data see Appendix D, Supporting Information).

4.3 Reaction Mechanism

In the upgrading scheme investigated in this perspective, the reduced metal oxide acts as a well of reduction potential, which is drawn upon by reactions with bio-oil oxygenates occurring at the surface until the reduced metal oxide is completely re-oxidized and its reduction potential is exhausted. Experimentally, the direct deoxygenation of acetic acid to acetaldehyde during reaction with zinc metal demonstrated comparable selectivities with the analogous HDO of acetic acid over a zinc oxide catalyst. Although there is still debate and the detailed mechanisms are unclear, many researchers have suggested that HDO of oxygenate species on metal-oxide catalysts or oxide-supported transition metal catalysts generally occurs by a Mars-van Krevelen mechanism [34, 36, 73, 82, 93, 94], in which the creation and destruction of surface oxygen vacancies are responsible for oxygen removal from the adsorbed species. This suggestion has recently been corroborated by theoretical studies [35, 98] in which vacancy-assisted mechanisms for HDO on MoO_3 were demonstrated to have lower energy barriers than direct hydrogen transfer pathways.

A comparison of the experimental results of Zn/ZnO-catalyzed LOC and HDO gives strong support for the growing consensus that metal-oxide catalyzed HDO occurs via a Mars-van Krevelen mechanism, in which the active sites of the reaction are coordinatively-unsaturated metal surface sites (*i.e.* oxygen vacancies). The results demonstrate that zero-valent zinc metal is capable of direct deoxygenation of acetic acid to acetaldehyde in the absence of H_2 and, furthermore, that the activity of this reaction decays as it progresses and the zinc metal surface is oxidized.

A commonly proposed mechanism of HDO over metal oxide catalysts is essentially the reverse of that in selective oxidation, for which an extensive body of literature exists [99–101]. The mechanism of metal-oxide catalyzed HDO of a carboxylic acid is illustrated on the left-hand side of Figure 6. In step **(1)**, the reaction of one molecule of H_2 with a lattice oxygen atom in the oxide catalyst (*i.e.*, zinc oxide) produces a molecule of water and leaves behind a single oxygen vacancy. The carboxylic acid species subsequently adsorbs onto the surface, filling in the vacancy with its own hydroxyl oxygen atom **(2)**. This is followed by the transfer of a metal oxide surface hydroxyl hydrogen atom onto the central carbon atom **(3)**, effectively forming an adsorbed aldehyde. In the final step **(4)**, the aldehyde desorbs, leaving the surface restored to its original state.

Based on the experimental selectivity results discussed earlier, it is likely that the LOC upgrading reaction of a carboxylic acid with a zero-valent metal (*e.g.*, zinc metal) or low-valence metal oxide occurs through a similar mechanism. The crucial distinction would be the source of oxygen vacancies: whereas oxygen vacancies in the HDO mechanism derive from the reaction of a lattice oxygen atom with gas phase H_2, in the LOC mechanism oxygen vacancies could diffuse from the reduced bulk of the catalyst particle through the formed high-valence oxide front (*e.g.*, zinc oxide) to the surface where they would play the same role. The precise diffusion mechanism responsible for oxidation will depend on the structure of the metal oxide considered [105]. While the zero-valent metal or low-valence metal oxide catalyst in its initial reduced state has no higher-valence oxide front (*i.e.*, the entire surface is in a coordinatively unsaturated state), such a front would quickly develop and gradually increase in thickness as the reaction proceeds. This suggested LOC mechanism is illustrated in the right-hand side of Figure 6. In step **(1)**, a vacancy diffuses from the bulk to form a surface vacancy; steps **(2)**-**(4)** are identical to those in the HDO case.

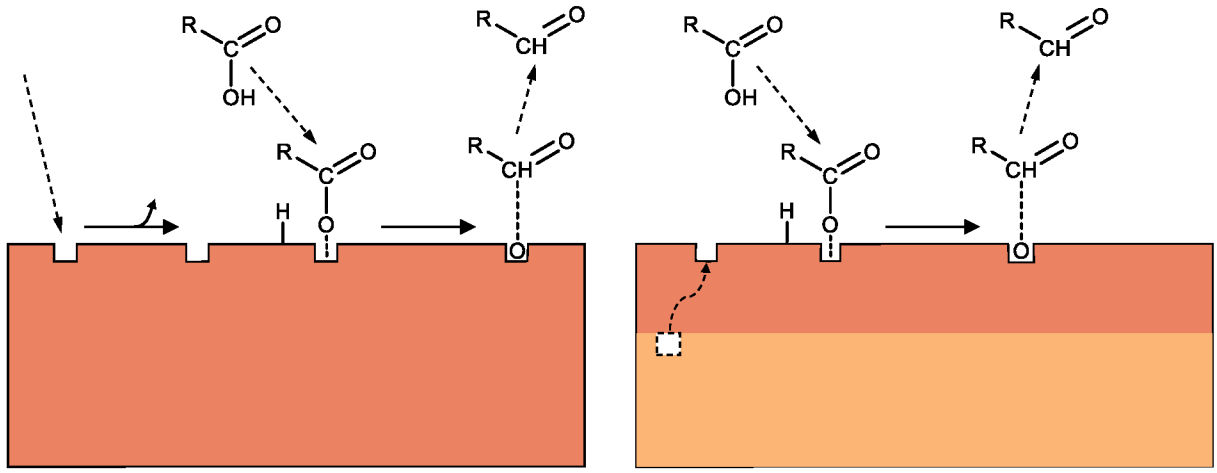

Figure 6: Generalized mechanism of carboxylic acid deoxygenation in looped-oxide catalysis, compared with the Mars-van Krevelen mechanism for hydrodeoxygenation, drawing from information provided in references: [89, 102–104]

5 Conclusion

Liquefaction and pyrolysis bio-oils represent promising feedstocks for renewable liquid transportation fuels. However, due to the low energy content of such bio-oils, it is advantageous to drive their deoxygenative upgrading with external renewable energy sources. In this perspective we have investigated a novel bio-oil upgrading pathway, looped-oxide catalysis (LOC), which harnesses solar thermal energy to drive bio-oil deoxygenation through the thermochemical cycling of a metal oxide; this metal oxide serves the dual function of catalytic surface and bulk reducing agent. Experimental results indicate that zero-valent zinc metal exhibits deoxygenation with selectivity comparable with that of hydrodeoxygenation (HDO) on zinc oxide. In addition to demonstrating the possibility of LOC upgrading, the selectivity results also suggest that both LOC and HDO operate via a vacancy-assisted Mars-van Krevelen mechanism in the Zn/ZnO system. LOC draws from the conceptual and technological framework of two existing processes, catalytic hydroprocessing and solar thermochemical water splitting, and as such stands to benefit from the ongoing research in each of these fields. Although LOC will face many challenges in development to an industrial-scale process, particularly in materials handling and thermal management, it may have inherent advantages over catalytic HDO of bio-oils that makes LOC a strong candidate as a complementary or alternate process.

1. Hydroprocessing (HDO) catalysts are designed with the goal of achieving selectivity towards deoxygenation without unnecessary hydrogenation. LOC achieves this goal by removing H_2 from the process altogether, enabling deoxygenation while suppressing hydrogenation.

2. The efficiency of HDO is restricted by the generation and compression of H_2, while LOC is limited only by the solar thermal reduction of a metal oxide. Consequently, LOC exhibits best-case exergy efficiencies of 25 to 43%, while HDO with solar photovoltaic-generated hydrogen is limited by a best-case efficiency of around 30%, as discussed in Section 3.

3. HDO is typically operated at high pressures (100-200 bar [18]) and a high partial pressure of H_2, well in excess of the stoichiometrically specified amount. For example, Elliott *et al.* reported operating hydroprocessing at 35–420 mol H_2 per kg bio-oil, compared to a stoichiometrically required amount of 25 mol/kg for complete deoxygenation [106]. The high partial pressure of H_2 is argued to increase the reaction rate and decrease catalyst coking by effecting a higher availability of hydrogen in the vicinity of the catalyst [89]. The LOC scheme may achieve the availability of oxygen vacancy sites on the metal oxide surface without requiring a high partial pressure of H_2, because these vacancies diffuse from within the reduced bulk of the oxide material itself.

4. An additional benefit of LOC is that the catalyst is renewed upon each iteration of the LOC cycle, avoiding the significant problem of long-term catalyst coking, which is prevalent in HDO processes [19–22, 30].

After decades of research, the field of solar-thermal processing is mature to the extent that the use of solar thermochemical cycles for bio-oil upgrading is technologically feasible and merits exploration. Augmented biomass-to-fuels pathways such as LOC, which incorporate externally-generated renewable energy into the final fuel product, have the potential to enable up to a threefold increase in fuel yield over standalone processes for a given quantity of biomass [4, 5]. Such a dramatic change will be necessary to achieve complete replacement of petroleum-derived fuels in the United States and other regions where hydrocarbon fuel consumption exceeds the local biomass production capacity. There are many more metal oxide redox cycles with acceptable bulk thermodynamics than the five candidates identified in this perspective, especially when more complex materials than the binary metal oxides are considered. A thorough understanding of the characteristics of bio-oil deoxygenation upon reaction with zero-valent metals and low-valence metal oxides will allow for greater precision in achieving LOC deoxygenation and, in turn, can inform the design of better HDO catalysts by elucidating the role of surface oxygen vacancies in facilitating oxygen removal from adsorbed species.

ASSOCIATED CONTENT

Supporting information. A supplemental document is provided containing Appendices A – D referenced in the text. This includes details of the exergy efficiency analysis discussed in Section 3, the raw data used in the generation of Figure 2 and experimental yields of acetic acid HDO and LOC products to complement the results provided in Section 4.2.

AUTHOR INFORMATION

Corresponding author. *Email: andrew_peterson@brown.edu. Telephone +1 401-863-2153.

Acknowledgments. The authors would like to thank the Institute for Molecular and Nanoscale Innovation and the DiMase Family for partially funding this study. The authors also wish to thank Benjamin Johnson and Szabolcs Harnos for their helpful contributions to the experimental setup.

References

[1] National Research Council. *Liquid Transportation Fuels from Coal and Biomass: Technological Status, Costs, and Environmental Impacts*. The National Academies Press, Washington, DC **2009**.

[2] Perlack, R.; Wright, L.; Turhollow, A.; Graham, R.; Stokes, B.; Erbach, D. Biomass as Feedstock for a Bioenergy and Bioproducts Industry: The Technical Feasibility of a Billion-Ton Annual Study. Technical report, U.S. Department of Energy / U.S. Department of Agriculture **2005**. DOE/GO-102995-2135, ORNL/TM-2005/66.

[3] U.S Department of Energy. *U.S. Billion-Ton Update: Biomass Supply for a Bioenergy and Bioproducts Industry*. Oak Ridge National Laboratory, Oak Ridge, TN. **2011**. ORNL/TM-2011/224.

[4] Dietenberger, M.; Anderson, M. Vision of the US biofuel future: a case for hydrogen-enriched biomass gasification. *Ind. Eng. Chem. Res.* **2007**; 46, 8863–8874.

[5] Singh, N.R.; Delgass, W.N.; Ribeiro, F.H.; Agrawal, R. Estimation of liquid fuel yields from biomass. *Environ. Sci. Technol.* **2010**; 44, 5298–305.

[6] Huo, Z.; Hu, M.; Zeng, X.; Yun, J.; Jin, F. Catalytic reduction of carbon dioxide into methanol over copper under hydrothermal conditions. *Catal. Today* **2012**; 194, 25–29.

[7] Xu, Y.; Wang, T.; Ma, L.; Zhang, Q.; Liang, W. Upgrading of the liquid fuel from fast pyrolysis of biomass over MoNi/γ-Al_2O_3 catalysts. *Appl. Energy* **2010**; 87, 2886–2891.

[8] Jin, F.; Gao, Y.; Jin, Y.; Zhang, Y.; Cao, J.; Wei, Z.; Smith Jr, R.L. High-yield reduction of carbon dioxide into formic acid by zero-valent metal/metal oxide redox cycles. *Energy Environ. Sci.* **2011**; 4, 881.

[9] Stamatiou, A.; Loutzenhiser, P.G.; Steinfeld, A. Solar Syngas Production from H_2O and CO_2 via Two-Step Thermochemical Cycles Based on Zn/ZnO and FeO/Fe_3O_4 Redox Reactions: Kinetic Analysis. *Energy & Fuels* **2010**; 24, 2716–2722.

[10] Liu, W.J.; Zhang, X.S.; Qv, Y.C.; Jiang, H.; Yu, H.Q. Bio-oil upgrading at ambient pressure and temperature using zero valent metals. *Green Chem.* **2012**; 14, 2226–2233.

[11] Yao, H.; Xu, Z.; Cheng, M.; Yun, J.; Jing, Z.; Jin, F. Catalytic conversion of formic acid to methanol with Cu and Al under hydrothermal conditions. *BioResources* **2012**; 7, 972–983.

[12] Furler, P.; Scheffe, J.; Gorbar, M.; Moes, L. Solar thermochemical CO_2 splitting utilizing a reticulated porous ceria redox system. *Energy & Fuels* **2012**; 26, 7051–7059.

[13] Scheffe, J.R.; Steinfeld, A. Thermodynamic Analysis of Cerium-Based Oxides for Solar Thermochemical Fuel Production. *Energy & Fuels* **2012**; 26, 1928–1936.

[14] Scheffe, J.; Jacot, R. Synthesis, Characterization, and Thermochemical Redox Performance of Hf^{4+}, Zr^{4+}, and Sc^{3+} Doped Ceria for Splitting CO_2. *J. Phys. Chem. C* **2013**; 117, 24104–24114.

[15] Michalsky, R.; Pfromm, P.H. Chromium as reactant for solar thermochemical synthesis of ammonia from steam, nitrogen, and biomass at atmospheric pressure. *Sol. Energy* **2011**; 85, 2642–2654.

[16] Michalsky, R.; Pfromm, P.H. An Ionicity Rationale to Design Solid phase Metal Nitride Reactants for Solar Ammonia Production. *J. Phys. Chem. C* **2012**; 116, 23243–23251.

[17] Elliott, D. Historical developments in hydroprocessing bio-oils. *Energy & Fuels* **2007**; 21, 1792–1815.

[18] Peterson, A.A.; Vogel, F.; Lachance, R.P.; Fröling, M.; Antal, Jr., M.J.; Tester, J.W. Thermochemical biofuel production in hydrothermal media: A review of sub- and supercritical water technologies. *Energy Environ. Sci.* **2008**; 1, 32.

[19] Furimsky, E.; Massoth, F. Deactivation of hydroprocessing catalysts. *Catal. Today* **1999**; 52, 381–495.

[20] Zhao, H.; Li, D.; Bui, P.; Oyama, S. Hydrodeoxygenation of guaiacol as model compound for pyrolysis oil on transition metal phosphide hydroprocessing catalysts. *Appl. Catal. A Gen.* **2011**; 391, 305–310.

[21] Boda, L.; Onyestyák, G.; Solt, H.; Lónyi, F.; Valyon, J.; Thernesz, A. Catalytic hydroconversion of tricaprylin and caprylic acid as model reaction for biofuel production from triglycerides. *Appl. Catal. A Gen.* **2010**; 374, 158–169.

[22] Popov, A.; Kondratieva, E. Bio-oils Hydrodeoxygenation: Adsorption of Phenolic Molecules on Oxidic Catalyst Supports. *J. Phys. Chem. C* **2010**; 114, 15661–15670.

[23] Elliott, D.; Schiefelbein, G. Liquid hydrocarbon fuels from biomass. *American Chemical Society, Division of Fuel Chemistry Annual Meeting Preprints* **1989**; 34, 1160–1166.

[24] Czernik, S.; Bridgwater, A.V. Overview of applications of biomass fast pyrolysis oil. *Energy & Fuels* **2004**; 18, 590–598.

[25] Bridgwater, A. Review of fast pyrolysis of biomass and product upgrading. *Biomass and Bioenergy* **2012**; 38, 68–94.

[26] Mohan, D.; Pittman, C.U.; Steele, P.H. Pyrolysis of Wood/Biomass for Bio-oil: A Critical Review. *Energy & Fuels* **2006**; 20, 848–889.

[27] Centi, G.; van Santen, R.A. *Catalysis for Renewables: From Feedstock to Energy Production*. Wiley **2007**. ISBN 9783527317882.

[28] Lin, Y.C.; Li, C.L.; Wan, H.P.; Lee, H.T.; Liu, C.F. Catalytic Hydrodeoxygenation of Guaiacol on Rh-Based and Sulfided CoMo and NiMo Catalysts. *Energy & Fuels* **2011**; 25, 890–896.

[29] Senol, O.; Ryymin, E.M.; Viljava, T.R.; Krause, A. Effect of hydrogen sulphide on the hydrodeoxygenation of aromatic and aliphatic oxygenates on sulphided catalysts. *J. Mol. Catal. A Chem.* **2007**; 277, 107–112.

[30] Furimsky, E. Catalytic hydrodeoxygenation. *Appl. Catal. A Gen.* **2000**; 199, 147–190.

[31] Serrano-Ruiz, J.C.; Braden, D.J.; West, R.M.; Dumesic, J.A. Conversion of cellulose to hydrocarbon fuels by progressive removal of oxygen. *Appl. Catal. B Environ.* **2010**; 100, 184–189.

[32] Ferrari, M. Influences of the Hydrogen Sulfide Partial Pressure and of a Nitrogen Compound on the Hydrodeoxygenation Activity of a CoMo/Carbon Catalyst. *J. Catal.* **2001**; 198, 47–55.

[33] Fisk, C.A.; Morgan, T.; Ji, Y.; Crocker, M.; Crofcheck, C.; Lewis, S.A. Bio-oil upgrading over platinum catalysts using in situ generated hydrogen. *Appl. Catal. A Gen.* **2009**; 358, 150–156.

[34] Mars, P.; van Krevelen, D. Oxidations carried out by means of vanadium oxide catalysts. *Chem. Eng. Sci.* **1954**; 3, 41–59.

[35] Mei, D.; Karim, A.; Wang, Y. Density Functional Theory Study of Acetaldehyde Hydrodeoxygenation on MoO_3. *J. Phys. Chem. C* **2011**; 115, 8155–8164.

[36] Prasomsri, T.; Nimmanwudipong, T.; Román-Leshkov, Y. Effective hydrodeoxygenation of biomass-derived oxygenates into unsaturated hydrocarbons by MoO_3 using low H_2 pressures. *Energy Environ. Sci.* **2013**; 6, 1732.

[37] Bunch, A.Y.; Wang, X.; Ozkan, U.S. Adsorption characteristics of reduced Mo and NiMo catalysts in the hydrodeoxygenation of benzofuran. *Appl. Catal. A Gen.* **2008**; 346, 96–103.

[38] Fletcher, E.A.; Moen, R.L. Hydrogen and oxygen from water. *Science* **1977**; 197, 1050–6.

[39] Scholl, K.L.; Fletcher, E.A. Y_2O_3-doped ZrO_2 membranes for solar electrothermal and solarthermal separations - II. Electron hole conductivity of yttria-stabilized zirconia. *Energy* **1993**; 18, 69.

[40] Ihara, S. Feasibility of hydrogen production by direct water splitting at high temperature. *Int. J. Hydrogen Energy* **1978**; 3, 287–296.

[41] Steinfeld, A. Solar hydrogen production via a two-step water-splitting thermochemical cycle based on Zn/ZnO redox reactions. *Int. J. Hydrogen Energy* **2002**; 27, 611–619.

[42] Wegner, K.; Ly, H.; Weiss, R.; Pratsinis, S.; Steinfeld, A. In situ formation and hydrolysis of Zn nanoparticles for H_2 production by the 2-step ZnO/Zn water-splitting thermochemical cycle. *Int. J. Hydrogen Energy* **2006**; 31, 55–61.

[43] Venstrom, L.; Krueger, K.; Leonard, N.; Tomlinson, B.; Duncan, S.; Palumbo, R.D. Solar Thermal Electrolytic Process for the Production of Zn From ZnO: An Ionic Conductivity Study. *J. Sol. Energy Eng.* **2009**; 131, 031005.

[44] Fletcher, E.A.; Macdonald, F.J.; Kunnerth, D. High temperature solar electrothermal processing — II. Zinc from zinc oxide. *Energy* **1985**; 8, 247–254.

[45] Scheffe, J.R.; Allendorf, M.D.; Coker, E.N.; Jacobs, B.W.; McDaniel, A.H.; Weimer, A.W. Hydrogen Production via Chemical Looping Redox Cycles Using Atomic Layer Deposition-Synthesized Iron Oxide and Cobalt Ferrites. *Chem. Mater.* **2011**; 23, 2030–2038.

[46] Gillot, B.; Guendouzi, M.E.; Laarj, M. Particle size effects on the oxidation–reduction behavior of Mn_3O_4 hausmannite. *Mater. Chem. Phys.* **2001**; 70, 54–60.

[47] Charvin, P.; Abanades, S.; Lemont, F.; Flamant, G. Experimental study of SnO_2/SnO/Sn thermochemical systems for solar production of hydrogen. *AIChE J.* **2008**; 54, 2759–2767.

[48] Abanades, S. CO_2 and H_2O reduction by solar thermochemical looping using SnO_2/SnO redox reactions: Thermogravimetric analysis. *Int. J. Hydrogen Energy* **2012**; 37, 8223–8231.

[49] Chueh, W.C.; Haile, S.M. A thermochemical study of ceria: exploiting an old material for new modes of energy conversion and CO2 mitigation. *Philos. Trans. A. Math. Phys. Eng. Sci.* **2010**; 368, 3269–94.

[50] Kreider, P.B.; Funke, H.H.; Cuche, K.; Schmidt, M.; Steinfeld, A.; Weimer, A.W. Manganese oxide based thermochemical hydrogen production cycle. *Int. J. Hydrogen Energy* **2011**; 36, 7028–7037.

[51] Sturzenegger, M.; Nüesch, P. Efficiency analysis for a manganese-oxide-based thermochemical cycle. *Energy* **1999**; 24, 959–970.

[52] Fletcher, E.A. Solarthermal Processing: A Review. *J. Sol. Energy Eng.* **2001**; 123, 63.

[53] Perret, R. Solar Thermochemical Hydrogen Production Research (STCH) Thermochemical Cycle Selection and Investment Priority. *Sandia Rep.* **2011**; .

[54] Steinfeld, A. Solar thermochemical production of hydrogen–A review. *Sol. Energy* **2005**; 78, 603–615.

[55] Krenzke, P.; Krueger, K.; Leonard, N.; Duncan, S.; Palumbo, R.D.; Moller, S. A Solar Thermal Electrolytic Reactor for Studying the Production of Metals From Their Oxides. *J. Sol. Energy Eng.* **2010**; 132, 034501.

[56] Fletcher, E.; Noring, J. High temperature solar electrothermal processing — Zinc from zinc oxide. *Energy* **1983**; 8, 247–254.

[57] Palumbo, R.; Fletcher, E. High temperature solar electrothermal processing—III. Zinc from zinc oxide at 1200–1675K using a non-consumable anode. *Energy* **1988**; 13, 319–332.

[58] Fletcher, E.A. Solarthermal and Solar Quasi-Electrolytic Processing and Separations: Zinc from Zinc Oxide as an Example. *Ind. Eng. Chem. Res.* **1999**; 38, 2275–2282.

[59] Chen, H.; Chang, J. Identifying the O_2 diffusion and reduction mechanisms on CeO_2 electrolyte in solid oxide fuel cells: A DFT+U study. *J. Comput. Chem.* **2009**; 30, 2433–2442.

[60] Schroeder, R.; Matthews, L.; Leatzow, D.; Kondratko, J.; Will, J.; Duncan, S.; Sheline, W.; Lindeke, N.; Palumbo, R.; Neves, P. Solar Thermal Electrolytic Process for the Production of Zn From ZnO: The Electrolysis of ZnO From 1275–1500 K. *J. Sol. Energy Eng.* **2011**; 133, 041013.

[61] *Ullmann's Encyclopedia of Industrial Chemistry*. Number 38 in Ullmann's Encyclopedia of Industrial Chemistry. John Wiley & Sons **2003**. ISBN 9783527303854.

[62] Bligaard, T.; Nørskov, J.; Dahl, S.; Matthiesen, J.; Christensen, C.; Sehested, J. The Brønsted–Evans–Polanyi relation and the volcano curve in heterogeneous catalysis. *J. Catal.* **2004**; 224, 206–217.

[63] Barin, I. Thermochemical Data of Pure Substances. *VCH Wienheim, Germany* **1989**; 1.

[64] Chase, M.W.; Davis, C.A.; Downey, J.R.; Frurip, D.J.; McDonald, R.A.; Syverud, A.N. JANAF Thermochemical Tables, 3rd ed. *Journal of Physical and Chemical Reference Data* **1985**; 14.

[65] Nakamura, T. Hydrogen production from water utilizing solar heat at high temperatures. *Sol. Energy* **1977**; 19, 467–475.

[66] Vesborg, P.C.K.; Jaramillo, T.F. Addressing the terawatt challenge: scalability in the supply of chemical elements for renewable energy. *RSC Adv.* **2012**; 2, 7933–7947.

[67] Tamaura, Y. Production of solar hydrogen by a novel, 2-step, water-splitting thermochemical cycle. *Energy* **1995**; 20, 325–330.

[68] Xiao, L.; Wu, S.Y.; Li, Y.R. Advances in solar hydrogen production via two-step water-splitting thermochemical cycles based on metal redox reactions. *Renewable Energy* **2012**; 41, 1–12.

[69] Fresno, F.; Fernández-Saavedra, R.; Belén Gómez-Mancebo, M.; Vidal, A.; Sánchez, M.; Isabel Rucandio, M.; Quejido, A.J.; Romero, M. Solar hydrogen production by two-step thermochemical cycles: Evaluation of the activity of commercial ferrites. *Int. J. Hydrogen Energy* **2009**; 34, 2918–2924.

[70] Ada, J.; Diego, L.F.D.; Garc, F.; Gaya, P.; Abad, A.; Casta, M.L. Selection of Oxygen Carriers for Chemical-Looping Combustion. *Energy and Fuels* **2004**; 18, 371–377.

[71] Tofighi, A.; Sibieude, F. Dissociation of magnetite in a solar furnace for hydrogen production. Tentative production evaluation of a 1000 kW concentrator from small scale (2 kW) experimental results. *Int. J. Hydrogen Energy* **1984**; 9, 293–296.

[72] Weidenkaff, A.; Nüesch, P.; Wokaun, A.; Reller, A. Mechanistic studies of the water-splitting reaction for producing solar hydrogen. *Solid state ionics* **1997**; 103, 915–922.

[73] Pestman, R.; Koster, R. Identification of the active sites in the selective hydrogenation of acetic acid to acetaldehyde on iron oxide catalysts. *J. Catal.* **1998**; 174, 142–152.

[74] Joshi, N.; Lawal, A. Hydrodeoxygenation of acetic acid in a microreactor. *Chem. Eng. Sci.* **2012**; 84, 761–771.

[75] Villasmil, W.; Brkic, M.; Wuillemin, D.; Meier, A.; Steinfeld, A. Pilot Scale Demonstration of a 100-kW_{th} Solar Thermochemical Plant for the Thermal Dissociation of ZnO. *J. Sol. Energy Eng.* **2013**; 136, 011017.

[76] Hölderich, W.; Tjoe, J. Direct hydrogenation of aromatic carboxylic acids to their corresponding aldehydes with zinc oxide catalysts. *Appl. Catal. A Gen.* **1999**; 184, 257–264.

[77] Wong, B. Solar Cadmium Hydrogen Production Cycle. Technical Report 1, Department of Energy Hydrogen Program **2009**.

[78] Petrus, L.; Noordermeer, M.A. Biomass to biofuels, a chemical perspective. *Green Chem.* **2006**; 8, 861.

[79] Alves, M. Cadmium Compounds as Catalysts for Biodiesel Production. *Ind. Eng. Chem. Res.* **2010**; 49, 7176–7182.

[80] Villafan-Vidales, H.I.; Arancibia-Bulnes, C.A.; Abanades, S.; Riveros-Rosas, D.; Romero-Paredes, H. Monte Carlo Heat Transfer Modeling of a Particle-Cloud Solar Reactor for SnO_2 Thermal Reduction. *J. Sol. Energy Eng.* **2011**; 133, 041009.

[81] He, Z.; Wang, X. Hydrodeoxygenation of model compounds and catalytic systems for pyrolysis bio-oils upgrading. *Catal. Sustain. Energy* **2012**; 1, 28–52.

[82] Pestman, R.; Koster, R.; Pieterse, J.; Ponec, V. Reactions of carboxylic acids on oxides: 1. Selective hydrogenation of acetic acid to acetaldehyde. *J. Catal.* **1997**; 264, 255–264.

[83] Chueh, W.C.; Falter, C.; Abbott, M.; Scipio, D.; Furler, P.; Haile, S.M.; Steinfeld, A. High-flux solar-driven thermochemical dissociation of CO_2 and H_2O using nonstoichiometric ceria. *Science* **2010**; 330, 1797–801.

[84] Shao, Z.; Haile, S.M. A high-performance cathode for the next generation of solid-oxide fuel cells. *Nature* **2004**; 431, 170–3.

[85] Abanades, S.; Flamant, G. Thermochemical hydrogen production from a two-step solar-driven water-splitting cycle based on cerium oxides. *Sol. Energy* **2006**; 80, 1611–1623.

[86] Chueh, W.C.; Haile, S.M. Electrochemistry of mixed oxygen ion and electron conducting electrodes in solid electrolyte cells. *Annu. Rev. Chem. Biomol. Eng.* **2012**; 3, 313–41.

[87] Sakata, Y.; Ponec, V. Reduction of benzoic acid on CeO_2 and, the effect of additives. *Appl. Catal. A Gen.* **1998**; 166, 173–184.

[88] Heaton, E.A.; Clifton-Brown, J.; Voigt, T.B.; Jones, M.B.; Long, S.P. Miscanthus for renewable energy generation: European Union experience and projections for Illinois. *Mitig. Adapt. Strateg. Glob. Chang.* **2004**; 9, 433–451.

[89] Mortensen, P.; Grunwaldt, J.D.; Jensen, P.; Knudsen, K.; Jensen, A. A review of catalytic upgrading of bio-oil to engine fuels. *Appl. Catal. A Gen.* **2011**; 407, 1–19.

[90] Zhang, Q.; Chang, J.; Wang, T.; Xu, Y. Review of biomass pyrolysis oil properties and upgrading research. *Energy Convers. Manag.* **2007**; 48, 87–92.

[91] Yakovlev, V.; Khromova, S.; Sherstyuk, O.; Dundich, V.; Ermakov, D.; Novopashina, V.; Lebedev, M.; Bulavchenko, O.; Parmon, V. Development of new catalytic systems for upgraded bio-fuels production from bio-crude-oil and biodiesel. *Catal. Today* **2009**; 144, 362–366.

[92] Zhao, C.; Kou, Y.; Lemonidou, A.A.; Li, X.; Lercher, J.A. Highly selective catalytic conversion of phenolic bio-oil to alkanes. *Angew. Chem. Int. Ed.* **2009**; 48, 3987–90.

[93] Yokoyama, T.; Yamagata, N. Hydrogenation of carboxylic acids to the corresponding aldehydes. *Appl. Catal. A Gen.* **2001**; 221, 227–239.

[94] Rachmady, W.; Vannice, M. Acetic acid hydrogenation over supported platinum catalysts. *J. Catal.* **2000**; 192, 322–334.

[95] Onyestyák, G.; Harnos, S.; Kaszonyi, A.; Štolcová, M.; Kalló, D. Acetic acid hydroconversion to ethanol over novel InNi/Al_2O_3 catalysts. *Catal. Commun.* **2012**; 27, 159–163.

[96] Perkins, C. Likely near-term solar-thermal water splitting technologies. *Int. J. Hydrogen Energy* **2004**; 29, 1587–1599.

[97] Nokkosmäki, M.; Kuoppala, E. Catalytic conversion of biomass pyrolysis vapours with zinc oxide. *J. Anal. Appl. Pyrolysis* **2000**; 55, 119–131.

[98] Moberg, D.; Thibodeau, T. Mechanism of Hydrodeoxygenation of Acrolein on a Cluster Model of MoO_3. *J. Phys. Chem. C* **2010**; 114, 13782–13795.

[99] Grasselli, R. Fundamental principles of selective heterogeneous oxidation catalysis. *Top. Catal.* **2002**; 21, 79–88.

[100] Doornkamp, C.; Ponec, V. The universal character of the Mars and Van Krevelen mechanism. *J. Mol. Catal. A Chem.* **2000**; 162, 19–32.

[101] Jackson, S.; Hargreaves, J. *Metal oxide catalysis* **2009**. ISBN 9783527316649.

[102] Mendes, M.; Santos, O.; Jordão, E.; Silva, A. Hydrogenation of oleic acid over ruthenium catalysts. *Appl. Catal. A Gen.* **2001**; 217, 253–262.

[103] Stakheev, A.; Kustov, L. Effects of the support on the morphology and electronic properties of supported metal clusters: modern concepts and progress in 1990s. *Appl. Catal. A Gen.* **1999**; 188, 3–35.

[104] Henrich, V.E.; Cox, P.A. *The Surface Science of Metal Oxides*. Cambridge University Press **1996**. ISBN 0521566878.

[105] Van Orman, J.A.; Crispin, K.L. Diffusion in Oxides. *Rev. Mineral. Geochemistry* **2010**; 72, 757–825.

[106] Elliott, D. Catalytic hydroprocessing of biomass fast pyrolysis bio-oil to produce hydrocarbon products. *Environ. Prog. Sustain. Energy* **2009**; 28, 441–449.

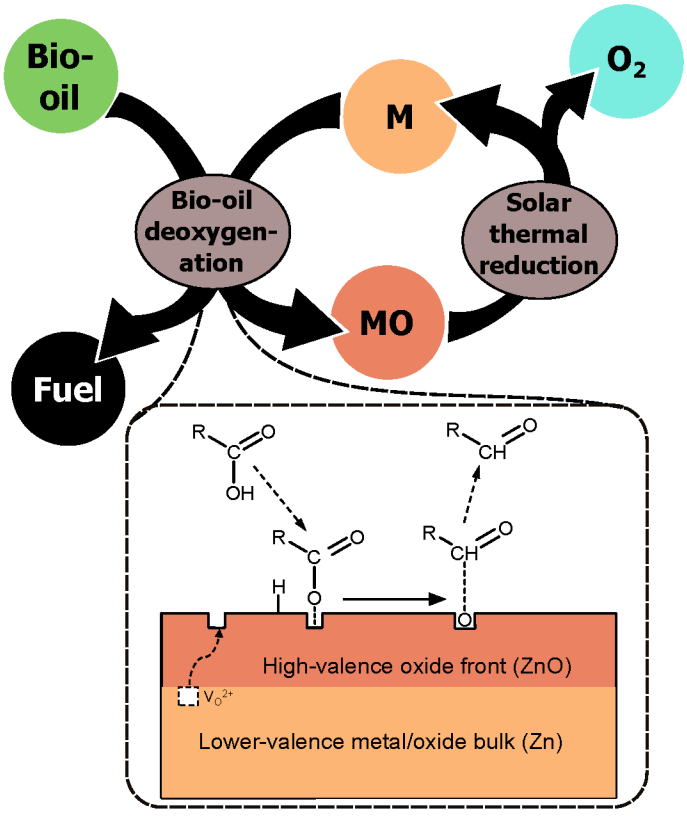

Looped-Oxide Catalysis: A Solar Thermal Approach to Bio-Oil Deoxygenation (Supporting Information)

Cory Hargus, Ronald Michalsky †, Andrew A. Peterson*

School of Engineering, Brown University, Providence, Rhode Island, 02912, United States.
† *Current address: Institute of Energy Technology, ETH Zurich, ML K 23 Sonneggstr. 3 CH-8092, Zurich, Switzerland.*
* *Corresponding author: Andrew_Peterson@brown.edu*

Appendix A: Derivation of solar absorption efficiency

The starting point for assessing the efficiency of any thermochemical cycle (TC) is the Carnot efficiency, which describes the maximum theoretical efficiency of a heat engine operating between a heat source at temperature T_{h} and a heat sink at temperature T_{c}. (For a simple derivation of the Carnot efficiency model as it is applied to solar TCs, see Ewan and Allen [1].)

$$\eta_{\mathrm{carnot}} = 1 - \frac{T_{\mathrm{c}}}{T_{\mathrm{h}}} \tag{1}$$

The Carnot efficiency model may be further refined for the case of a TC operated within a solar cavity, where some of the solar flux into the cavity of the furnace is lost to re-radiation, according to the Stefan-Boltzmann Law. Assuming perfect optics, perfect insulation and absorptivity and emissivity approaching unity, the absorption efficiency of a black body cavity is:

$$\eta_{\mathrm{absorption}} = \frac{IC - \sigma T_{\mathrm{h}}^4}{IC} \tag{2}$$

Here *C* denotes the "concentration ratio", which is a measure of the increase in solar flux intensity after amplification through the use of mirrors or condensing lenses. *I* represents the normal beam intensity of sunlight, taken to be 1 kW/m^2, and σ is the Stefan-Boltzmann constant. The maximum overall efficiency of a TC operated within a solar cavity is given by the product of the two efficiencies:

$$\eta_{\mathrm{overall}} = \eta_{\mathrm{carnot}} \times \eta_{\mathrm{absorption}} \tag{3}$$

Finally, by differentiating η_{overall} with respect to T_{h}, setting the resulting expression equal to zero and solving for *C*, we arrive at the analytical solution for the optimum concentration ratio corresponding to any given solar cavity temperature.

$$C_{\mathrm{optimum}} = \frac{\sigma T_{\mathrm{h}}^4 (4T_{\mathrm{h}} - 3T_{\mathrm{c}})}{I T_{\mathrm{c}}} \tag{4}$$

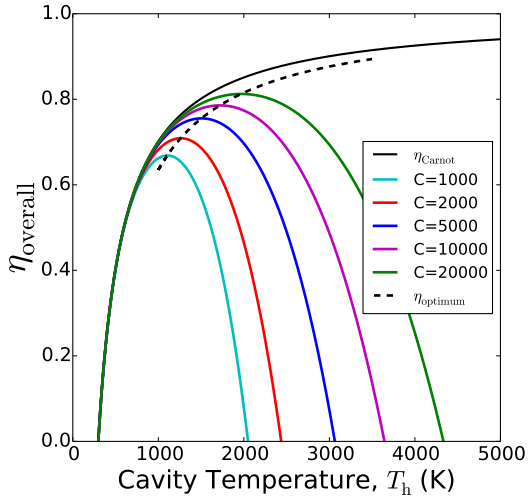

Figure 1: Overall efficiency of a solar furnace, η_{overall}, for select concentration ratios and optimum efficiency, η_{optimum}, as functions of temperature. Adapted from [2].

Figure 1 depicts the overall efficiency of a solar thermal metal oxide reduction process as a function of T_{h}, the cavity temperature. T_{c} has been set equal to 298 K and the overall efficiency is plotted along with the Carnot efficiency η_{optimum}, the efficiency of a solar cavity operating at the optimum concentration ratio, C_{optimum} for a given temperature. As the cavity temperature increases, η_{optimum} approaches the Carnot efficiency. The intersection of each efficiency curve with the x-axis is the stagnation temperature for a solar cavity operating at a given concentration ratio. This is the temperature at which the rate of absorption of solar thermal energy is in equilibrium with the rate of black-body re-radiation.

Appendix B: Exergy Analysis

To evaluate the theoretical performance of the five candidate looped-oxide catalysis (LOC) materials identified in Section 3, we have developed an exergy analysis for each material, with the goal of identifying areas of greatest loss and comparing between theoretical performances of the candidate oxide cycles. This analysis is modeled after the approach taken in [3]. Energy losses due to heat dissipation through the reactor walls and due to the circulation of an inert carrier gas and the operation of solids conveyors are neglected at this point. Consistent with the analysis presented in this perspective, the deoxygenation of acetic acid to acetaldehyde has been used as a model bio-oil deoxygenation reaction.

A flow diagram for the LOC process is presented in Figure 2. This schematic set up consists of a solar electrothermal furnace for the reduction of the metal oxide, a cooling device and an upgrading reactor in which acetic acid oxidizes the reduced metal oxide, reforming the higher-valence metal oxide and yielding the deoxygenated product, acetaldehyde. All steps are assumed to take place at 1 bar of total pressure.

The cycle begins with the solar heating of acetic acid to 500 K and the solar heating of the metal oxide to 1500 K, followed by dissociation of the metal oxide to the reduced oxide and oxygen gas. For many metal oxides, the limitations of current solar concentration optical systems and materials prohibit operation at the temperatures required for pure-thermal dissociation. Therefore,

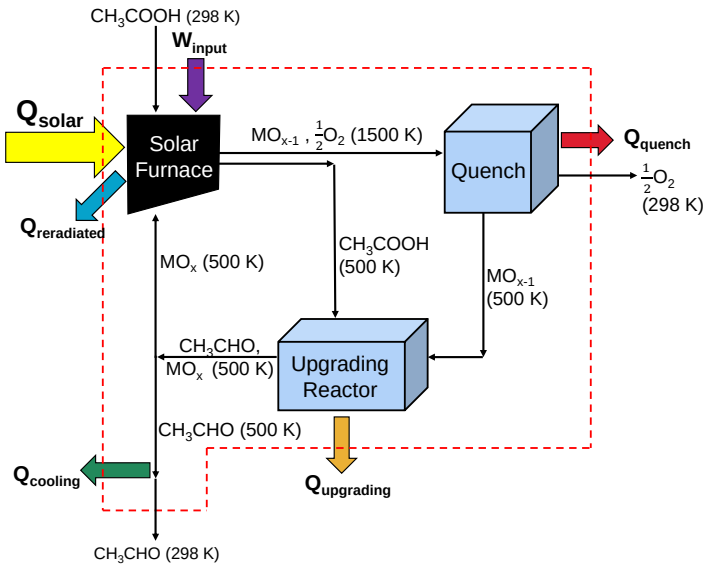

Figure 2: Flow diagram of the LOC upgrading of acetic acid to acetaldehyde used in the exergy analysis.

a solar furnace operating temperature of 1500 K is adopted in this analysis, where all additional work is added to the solar reactor via electrothermal reduction. The optimum concentration ratio corresponding to a cavity temperature of 1500 K is used: $C_{\text{optimum}} = 4920$. The three most common solar optical concentration setups, depicted in Figure 3, are parabolic trough, tower, and dish systems [4]. The parabolic trough concentrator, which can only achieve concentration ratios of 30 to 100, uses a linear parabolic optical reflector to concentrate sunlight onto a collector along the focal line of the trough. Although this concentration setup is generally incapable of reducing the metal oxides commonly used in water splitting and CO_2 splitting applications, it may find application in driving the reduction of weakly-bound metal oxides in LOC deoxygenation of alcohols, phenols, etc. In the tower arrangement, which exhibits typical concentration ratios of 500 to 1000, a field of dual-axis heliostats reflect sunlight onto a single focal point in a collecting tower. Finally, the dish collector can achieve concentration ratios of 1000-10000 and utilizes a parabolic dish reflector which tracks the sun along two axes, focusing sunlight onto a single receiving cavity at the focal point of the dish [5].

After reduction in the solar electrothermal furnace, the reduced oxide is cooled to 500 K while oxygen is vented from the cycle at 298 K. For the candidate oxides with gaseous or metastable reduction products (namely: Zn, Cd, FeO and SnO) this cooling step must involve rapid quenching to control particle nucleation size and phase stability. Therefore it is assumed in this analysis that no heat is recovered during quenching or cooling of products. In the next step, the reduced oxide is sent to the upgrading reactor where it is re-oxidized by acetic acid, rejecting additional heat from the cycle and yielding acetaldehyde, which exits the cycle at 298 K after additional cooling. By considering only the chemical inputs and outputs to the cycle enclosed in the dotted red line in Figure 2, it is easy to see that the net result of the cycle is the dissociation of acetic acid to form acetaldehyde and oxygen via the input of solar heat and electrolytic work.

$$\mathrm{CH_3COOH} \xrightarrow[\dot{W}_{\text{input}}]{\dot{Q}_{\text{solar}}} \mathrm{CH_3CHO} + \frac{1}{2}\mathrm{O_2} \tag{5}$$

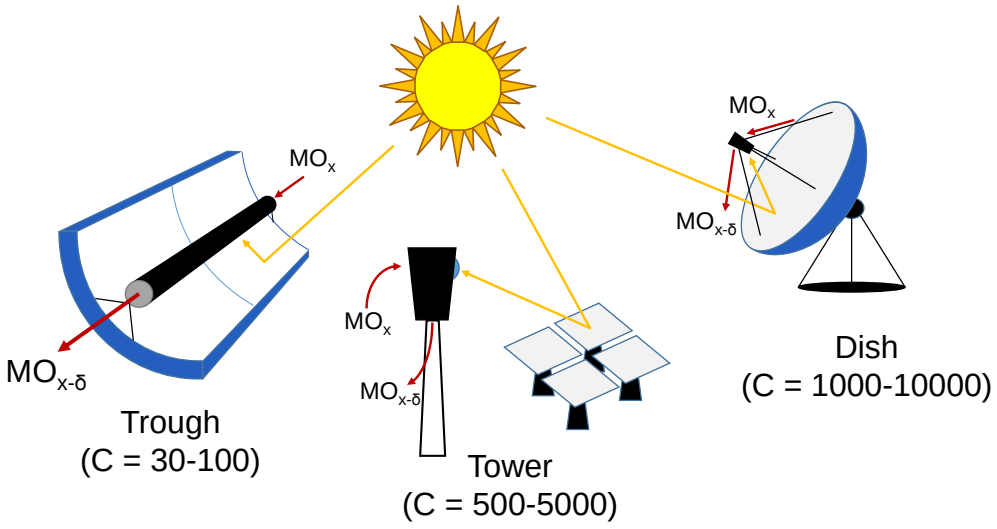

Figure 3: The three broad categories of solar collection schemes for the thermal reduction of metal oxides and typical ranges [4] of concentration ratios (C) achievable with each setup.

Therefore, the exergy efficiency of the process may be defined as:

$$\eta_{\text{exergy}} = \frac{\dot{n}_{\text{CH}_3\text{COOH}}\,\Delta\text{G}_{\text{rxn}}}{\dot{Q}_{\text{solar}} + \frac{\dot{W}_{\text{input}}}{\eta_{\text{PV}}}} \tag{6}$$

Here, $\dot{n}_{\text{CH}_3\text{COOH}}$ denotes the molar flow rate of acetic acid into the upgrading reactor, which is set equal to 1 mole/second and $\Delta\text{G}_{\text{rxn}}$ refers to the Gibbs free energy of the deoxygenation of one mole of acetic acid to acetaldehyde (Equation 5) at 298 K. $\dot{W}_{\text{input}}$ represents the additional work provided to the solar furnace to drive the metal oxide reduction reaction. For this analysis, we have assumed that this additional work is provided by an array of ideal p-n junction photovoltaic (PV) solar cells operating at the Shockley-Queisser limiting efficiency of $\eta_{\text{PV}} = 33.7\%$. $\dot{Q}_{\text{solar}}$ is the solar heat supplied to the reactor, and is given by the quotient of the total heat required by the solar reactor and the absorption efficiency (see Appendix A).

$$\dot{Q}_{\text{solar}} = \frac{1}{\eta_{\text{absorption}}}\Bigg[\dot{n}_{\text{MO}_\text{x}}\Delta\text{H}\,|_{\text{MO}_\text{x}(500\text{K})\rightarrow\text{MO}_{\text{x}-\delta}(1500\text{K})+\frac{\delta}{2}\text{O}_2(1500\text{K})} + \dot{n}_{\text{CH}_3\text{COOH}}\Delta\text{H}\,|_{\text{CH}_3\text{COOH}(298\text{K})\rightarrow\text{CH}_3\text{COOH}(500K)}\Bigg] \tag{7}$$

In the above equation, $\dot{n}_{\text{MO}_\text{x}}$ denotes the molar flow rate of metal oxide into the solar furnace, which is set equal to $\frac{1}{\delta}$ moles per second in order to balance the flow of acetic acid into the upgrading reactor. The exergy efficiencies of each of the candidate cycles are listed in Table 1. Also provided in Table 1 is the required heliostat and photovoltaic (PV) area of each cycle, assuming a solar tower collector as depicted in Figure 3. These quantities are defined as the solar collection areas required to gather sufficient solar thermal and electrical energy to drive each cycle at a rate of 1 mole of acetaldehyde produced per second.

Table 1: Efficiency analysis results for candidate LOC upgrading cycles.

Reaction Set	η_{exergy}	$\dot{W}_{\text{input}}$ (kW)	Heliostat Area (m^2)	PV Area (m^2)
$ZnO \rightarrow Zn + \frac{1}{2}O_2$ $CH_3COOH + Zn \rightarrow$ $CH_3CHO + ZnO$	27.5%	164	392	485
$CdO \rightarrow Cd + \frac{1}{2}O_2$ $CH_3COOH + Cd \rightarrow$ $CH_3CHO + CdO$	42.6%	62	382	185
$Fe_3O_4 \rightarrow 3\,FeO + \frac{1}{2}O_2$ $CH_3COOH + 3\,FeO \rightarrow$ $CH_3CHO + Fe_3O_4$	31.6%	420	764	344
$2\,CeO_2 \rightarrow Ce_2O_3 + \frac{1}{2}O_2$ $CH_3COOH + Ce_2O_3 \rightarrow$ $CH_3CHO + 2\,CeO_2$	25.8%	179	406	530
$SnO_2 \rightarrow SnO + \frac{1}{2}O_2$ $CH_3COOH + SnO \rightarrow$ $CH_3CHO + SnO_2$	26.9%	134	500	397

$$\text{Heliostat Area} = \frac{\dot{Q}_{\text{solar}}}{I} \tag{8}$$

$$\text{PV Area} = \frac{\dot{W}_{\text{input}}}{\eta_{\text{PV}} \times I} \tag{9}$$

We have also calculated the value of each heat loss term illustrated in Figure 2 for the five candidate cycles. Decomposing the heat transfer out of the TC into its constituent parts allows for a comparison of the relative contribution of each term. This is illustrated in Figure 4. Performing an energy balance on the cycle in Figure 2 (within the red dotted line) indicates that the solar heat, $\dot{Q}_{\text{solar}}$, balances with the sum of the heat loss terms plus the effective change in chemical enthalpy of the cycle in net, ΔH_{eff}, which is defined as the enthalpy of the net upgrading reaction at 298 K and 1 bar total pressure, minus the total electrical work added during the solar thermal reduction of the metal oxide.

$$\dot{Q}_{\text{solar}} = \dot{Q}_{\text{reradiated}} + \dot{Q}_{\text{quench}} + \dot{Q}_{\text{upgrading}} + \dot{Q}_{\text{cooling}} + \Delta H_{\text{eff}} \tag{10}$$

The net work accomplished by the cycle is indicated in Figure 4 by the distance between the dotted line and the top of each bar and is defined as follows:

$$\dot{W}_{\text{net}} = \dot{n}_{CH_3COOH} \Delta G_{\text{rxn}} - \dot{W}_{\text{input}} \tag{11}$$

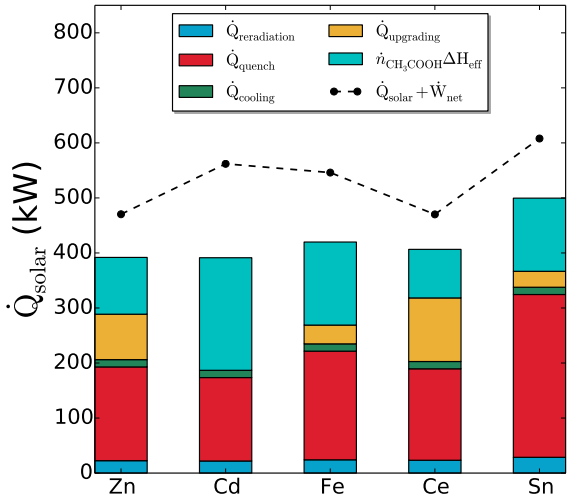

Figure 4: Heat loss terms in the exergy model for acetic acid selective deoxygenation to acetaldehyde, where the total height of each bar gives the total solar influx, $\dot{Q}_{\mathrm{solar}}$.

where ΔG_{rxn} again refers to the Gibbs free energy of the reaction at 298 K of one mole of acetic acid to acetaldehyde (Equation 5).

Due to the low solar furnace operation temperature of 1500 K, the re-radiation losses are relatively small, with most heat loss occurring during the quenching or cooling step. We have assumed here that no quenching heat is recovered; typical quenching parameters make any heat recovery difficult. Low-temperature heat lost during the upgrading reaction, the HDO reaction and product cooling constitutes a relatively small component of the total heat loss, and has also been assumed non-recoverable. In practice, a small amount of pumping work will be required due to pressure drops occurring between various stages of the cycle.

Appendix C: Thermochemical quantities

Table 2: Reaction stoichiometry and thermochemical values used in construction of Figure 2 of the main text. The metal-oxygen bond strength is defined as the ΔH of the reduction reaction, which is always normalized to the formation of $\frac{1}{2}$ moles of O_2. The Gibbs free energy of the metal oxide reduction and acetic acid deoxygenative upgrading reaction reactions are also provided in the columns labeled ΔG_r and ΔG_u, respectively. The final column lists the molecular weight ratio of the zero-valent metal or low-valence metal oxide to acetic acid in each reaction. This value is represented graphically in Figure 2 of the main text as the inverse of the weighting (size) of each point.

Metal Oxide Reduction	Bio-oil Upgrading	M-O Bond Strength (kJ/mol)	ΔG_r (kJ/mol)	ΔG_u (kJ/mol)	Metal/Acid wt. Ratio
$3Fe_2O_3 \rightarrow 2Fe_3O_4 + \frac{1}{2}O_2$	$2Fe_3O_4 + CH_3COOH \rightarrow 3Fe_2O_3 + CH_3CHO$	235.978	33.03686	51.50783	7.711365
$Fe_3O_4 \rightarrow 3FeO + \frac{1}{2}O_2$	$3FeO + CH_3COOH \rightarrow Fe_3O_4 + CH_3CHO$	302.251	111.9764	-12.9453	3.589227
$FeO \rightarrow Fe + \frac{1}{2}O_2$	$Fe + CH_3COOH \rightarrow FeO + CH_3CHO$	272.044	175.0502	-18.4222	0.929987
$\frac{1}{4}Fe_3O_4 \rightarrow \frac{3}{4}Fe + \frac{1}{2}O_2$	$\frac{3}{4}Fe + CH_3COOH \rightarrow \frac{1}{4}Fe_3O_4 + CH_3CHO$	279.5958	159.2817	-17.0529	0.69749
$Fe_2O_3 \rightarrow 2FeO + \frac{1}{2}O_2$	$2FeO + CH_3COOH \rightarrow Fe_2O_3 + CH_3CHO$	280.16	85.66321	6.77808	2.392818
$Mn_3O_4 \rightarrow 3MnO + \frac{1}{2}O_2$	$3MnO + CH_3COOH \rightarrow Mn_3O_4 + CH_3CHO$	232.136	43.97802	51.98201	3.543816
$MnO \rightarrow Mn + \frac{1}{2}O_2$	$Mn + CH_3COOH \rightarrow MnO + CH_3CHO$	385.221	274.3574	-128.072	0.91485
$\frac{1}{3}Cr_2O_3 \rightarrow \frac{2}{3}Cr + \frac{1}{2}O_2$	$\frac{2}{3}Cr + CH_3COOH \rightarrow \frac{1}{3}Cr_2O_3 + CH_3CHO$	379.9003	246.0345	-111.499	0.577239
$Al_2O_3 \rightarrow 2AlO + \frac{1}{2}O_2$	$2AlO + CH_3COOH \rightarrow Al_2O_3 + CH_3CHO$	1812.928	1153.696	-1391.26	1.431474
$2AlO \rightarrow Al_2O + \frac{1}{2}O_2$	$Al_2O + CH_3COOH \rightarrow 2AlO + CH_3CHO$	-267.777	-199.635	494.4735	1.165036
$Al_2O \rightarrow 2Al + \frac{1}{2}O_2$	$2Al + CH_3COOH \rightarrow Al_2O + CH_3CHO$	130.541	244.9732	39.18734	0.898631
$\frac{1}{3}Al_2O_3 \rightarrow \frac{2}{3}Al + \frac{1}{2}O_2$	$\frac{2}{3}Al + CH_3COOH \rightarrow \frac{1}{3}Al_2O_3 + CH_3CHO$	558.564	399.678	-285.866	0.299544
$MgO \rightarrow Mg + \frac{1}{2}O_2$	$Mg + CH_3COOH \rightarrow MgO + CH_3CHO$	601.241	424.4333	-327.406	0.404737
$CaO \rightarrow Ca + \frac{1}{2}O_2$	$Ca + CH_3COOH \rightarrow CaO + CH_3CHO$	635.089	478.3692	-362.569	0.667395
$SrO \rightarrow Sr + \frac{1}{2}O_2$	$Sr + CH_3COOH \rightarrow SrO + CH_3CHO$	592.036	443.2446	-322.398	1.459084
$BaO \rightarrow Ba + \frac{1}{2}O_2$	$Ba + CH_3COOH \rightarrow BaO + CH_3CHO$	553.543	397.4632	-284.152	2.286826
$ZnO \rightarrow Zn + \frac{1}{2}O_2$	$Zn + CH_3COOH \rightarrow ZnO + CH_3CHO$	350.46	162.8706	-78.2073	1.088901
$CdO \rightarrow Cd + \frac{1}{2}O_2$	$Cd + CH_3COOH \rightarrow CdO + CH_3CHO$	258.99	64.79342	9.619015	1.871914
$3TiO_2(R) \rightarrow Ti_3O_5 + \frac{1}{2}O_2$	$Ti_3O_5 + CH_3COOH \rightarrow 3TiO_2(R) + CH_3CHO$	375.095	213.7271	-112.972	3.724095
$2Ti_3O_5 \rightarrow 3Ti_2O_3 + \frac{1}{2}O_2$	$3Ti_2O_3 + CH_3COOH \rightarrow 2Ti_3O_5 + CH_3CHO$	355.64	255.3872	-98.1734	7.181752
$Ti_2O_3 \rightarrow 2TiO + \frac{1}{2}O_2$	$2TiO + CH_3COOH \rightarrow Ti_2O_3 + CH_3CHO$	435.554	310.6243	-199.619	2.127479
$TiO \rightarrow Ti + \frac{1}{2}O_2$	$Ti + CH_3COOH \rightarrow TiO + CH_3CHO$	542.665	403.0029	-258.969	0.797317
$\frac{1}{3}Ti_2O_3 \rightarrow \frac{2}{3}Ti + \frac{1}{2}O_2$	$\frac{2}{3}Ti + CH_3COOH \rightarrow \frac{1}{3}Ti_2O_3 + CH_3CHO$	506.9613	372.21	-239.185	0.531545
$\frac{1}{5}Ti_3O_5 \rightarrow \frac{3}{5}Ti + \frac{1}{2}O_2$	$\frac{3}{5}Ti + CH_3COOH \rightarrow \frac{1}{5}Ti_3O_5 + CH_3CHO$	491.8292	360.5277	-225.084	0.47839
$\frac{1}{2}TiO_2(R) \rightarrow \frac{1}{2}Ti + \frac{1}{2}O_2$	$\frac{1}{2}Ti + CH_3COOH \rightarrow \frac{1}{2}TiO_2(R) + CH_3CHO$	472.3735	336.061	-206.399	0.398659
$\frac{1}{2}Ti_3O_5 \rightarrow 3/2TiO + \frac{1}{2}O_2$	$3/2TiO + CH_3COOH \rightarrow \frac{1}{2}Ti_3O_5 + CH_3CHO$	415.5755	296.815	-174.257	1.595609
$TiO_2(R) \rightarrow TiO + \frac{1}{2}O_2$	$TiO + CH_3COOH \rightarrow TiO_2(R) + CH_3CHO$	402.082	269.119	-153.829	1.063739
$2TiO_2(R) \rightarrow Ti_2O_3 + \frac{1}{2}O_2$	$Ti_2O_3 + CH_3COOH \rightarrow 2TiO_2(R) + CH_3CHO$	368.61	227.6138	-108.039	2.393917
$ZrO_2 \rightarrow ZrO + \frac{1}{2}O_2$	$ZrO + CH_3COOH \rightarrow ZrO_2 + CH_3CHO$	1156.039	757.5717	-797.391	1.785521
$ZrO \rightarrow Zr + \frac{1}{2}O_2$	$Zr + CH_3COOH \rightarrow ZrO + CH_3CHO$	-58.576	16.15024	237.2453	1.519099
$\frac{1}{2}ZrO_2 \rightarrow \frac{1}{2}Zr + \frac{1}{2}O_2$	$\frac{1}{2}Zr + CH_3COOH \rightarrow \frac{1}{2}ZrO_2 + CH_3CHO$	548.7315	386.861	-280.073	0.75955
$\frac{1}{2}HfO_2 \rightarrow \frac{1}{2}Hf + \frac{1}{2}O_2$	$\frac{1}{2}Hf + CH_3COOH \rightarrow \frac{1}{2}HfO_2 + CH_3CHO$	572.371	421.6384	-289.721	1.486144
$CoO \rightarrow Co + \frac{1}{2}O_2$	$Co + CH_3COOH \rightarrow CoO + CH_3CHO$	237.944	129.0262	19.95768	0.981377
$2RhO_2 \rightarrow Rh_2O_3 + \frac{1}{2}O_2$	$Rh_2O_3 + CH_3COOH \rightarrow 2RhO_2 + CH_3CHO$	12.36	478.9023	46.19554	4.226532
$NiO \rightarrow Ni + \frac{1}{2}O_2$	$Ni + CH_3COOH \rightarrow NiO + CH_3CHO$	239.701	107.9597	25.9408	0.97733
$MoO_3 \rightarrow MoO_2 + \frac{1}{2}O_2$	$MoO_2 + CH_3COOH \rightarrow MoO_3 + CH_3CHO$	156.147	73.12376	99.49551	2.130493
$\frac{1}{2}MoO_2 \rightarrow \frac{1}{2}Mo + \frac{1}{2}O_2$	$\frac{1}{2}Mo + CH_3COOH \rightarrow \frac{1}{2}MoO_2 + CH_3CHO$	294.47	163.1467	-28.4742	0.798816
$GeO_2 \rightarrow GeO + \frac{1}{2}O_2$	$GeO + CH_3COOH \rightarrow GeO_2 + CH_3CHO$	533.711	132.842	-186.732	1.475553
$GeO \rightarrow Ge + \frac{1}{2}O_2$	$Ge + CH_3COOH \rightarrow GeO + CH_3CHO$	46.191	149.1889	144.3271	1.209132
$\frac{1}{2}GeO_2 \rightarrow \frac{1}{2}Ge + \frac{1}{2}O_2$	$\frac{1}{2}Ge + CH_3COOH \rightarrow \frac{1}{2}GeO_2 + CH_3CHO$	289.951	141.2166	-21.2024	0.604566
$SnO_2 \rightarrow SnO + \frac{1}{2}O_2$	$SnO + CH_3COOH \rightarrow SnO_2 + CH_3CHO$	295.053	142.3815	-21.8907	2.24323
$SnO \rightarrow Sn + \frac{1}{2}O_2$	$Sn + CH_3COOH \rightarrow SnO + CH_3CHO$	285.77	130.2814	-17.372	1.976808
$\frac{1}{2}SnO_2 \rightarrow \frac{1}{2}Sn + \frac{1}{2}O_2$	$\frac{1}{2}Sn + CH_3COOH \rightarrow \frac{1}{2}SnO_2 + CH_3CHO$	290.4115	137.9402	-19.6313	0.988404
$PbO \rightarrow Pb + \frac{1}{2}O_2$	$Pb + CH_3COOH \rightarrow PbO + CH_3CHO$	218.062	77.45839	51.18705	3.450379
$Nb_2O_5 \rightarrow 2NbO_2 + \frac{1}{2}O_2$	$2NbO_2 + CH_3COOH \rightarrow Nb_2O_5 + CH_3CHO$	309.616	194.3468	-53.1201	4.159939
$NbO_2 \rightarrow NbO + \frac{1}{2}O_2$	$NbO + CH_3COOH \rightarrow NbO_2 + CH_3CHO$	375.305	251.4668	-118.721	1.813547
$NbO \rightarrow Nb + \frac{1}{2}O_2$	$Nb + CH_3COOH \rightarrow NbO + CH_3CHO$	419.655	281.1146	-144.854	1.547109
$\frac{1}{2}NbO_2 \rightarrow \frac{1}{2}Nb + \frac{1}{2}O_2$	$\frac{1}{2}Nb + CH_3COOH \rightarrow \frac{1}{2}NbO_2 + CH_3CHO$	397.48	266.2907	-131.788	0.773554
$\frac{1}{5}Nb_2O_5 \rightarrow 2/5Nb + \frac{1}{2}O_2$	$2/5\ Nb + CH_3COOH \rightarrow \frac{1}{5}Nb_2O_5 + CH_3CHO$	379.9072	251.9019	-116.054	0.618844
$\frac{1}{3}Nb_2O_5 \rightarrow \frac{2}{3}NbO + \frac{1}{2}O_2$	$\frac{2}{3}NbO + CH_3COOH \rightarrow \frac{1}{3}Nb_2O_5 + CH_3CHO$	353.4087	232.4268	-96.854	1.209032
$Ta_2O_5 \rightarrow 2TaO_2 + \frac{1}{2}O_2$	$2TaO_2 + CH_3COOH \rightarrow Ta_2O_5 + CH_3CHO$	1644.312	975.7338	-1195.85	7.092162
$TaO_2 \rightarrow TaO + \frac{1}{2}O_2$	$TaO + CH_3COOH \rightarrow TaO_2 + CH_3CHO$	393.296	287.2902	-150.18	3.279642
$TaO \rightarrow Ta + \frac{1}{2}O_2$	$Ta + CH_3COOH \rightarrow TaO + CH_3CHO$	-192.464	-74.4166	387.0032	3.01322
$\frac{1}{5}Ta_2O_5 \rightarrow 2/5Ta + \frac{1}{2}O_2$	$2/5Ta + CH_3COOH \rightarrow \frac{1}{5}Ta_2O_5 + CH_3CHO$	409.1952	280.2962	-144.442	1.205288
$\frac{1}{3}Ta_2O_5 \rightarrow \frac{2}{3}TaO + \frac{1}{2}O_2$	$\frac{2}{3}TaO + CH_3COOH \rightarrow \frac{1}{3}Ta_2O_5 + CH_3CHO$	810.3013	516.7714	-498.738	2.186428

Oxide Reduction	Bio-oil Upgrading	M-O Bond Strength (kJ/mol)	ΔG_{red} (kJ/mol)	ΔG_{upg} (kJ/mol)	Metal/Acid wt. Ratio
$Li_2O \rightarrow 2Li + \frac{1}{2}O_2$	$2Li + CH_3COOH \rightarrow Li_2O + CH_3CHO$	598.73	399.7812	-316.603	0.231169
$\frac{1}{3}B_2O_3 \rightarrow \frac{2}{3}B + \frac{1}{2}O_2$	$\frac{2}{3}B + CH_3COOH \rightarrow \frac{1}{3}B_2O_3 + CH_3CHO$	423.9787	303.1768	-160.285	0.120019
$2CeO_2 \rightarrow Ce_2O_3 + \frac{1}{2}O_2$	$Ce_2O_3 + CH_3COOH \rightarrow 2CeO_2 + CH_3CHO$	381.163	78.78053	-71.0108	5.465787
$\frac{1}{3}Ce_2O_3 \rightarrow \frac{2}{3}Ce + \frac{1}{2}O_2$	$\frac{2}{3}Ce + CH_3COOH \rightarrow \frac{1}{3}Ce_2O_3 + CH_3CHO$	598.7303	703.414	-340.173	1.555502
$\frac{1}{2}CeO_2 \rightarrow \frac{1}{2}Ce + \frac{1}{2}O_2$	$\frac{1}{2}Ce + CH_3COOH \rightarrow \frac{1}{2}CeO_2 + CH_3CHO$	544.3385	390.1538	-272.883	1.166626
$\frac{1}{3}Ga_2O_3 \rightarrow \frac{2}{3}Ga + \frac{1}{2}O_2$	$\frac{2}{3}Ga + CH_3COOH \rightarrow \frac{1}{3}Ga_2O_3 + CH_3CHO$	363.0317	200.0468	-90.1847	0.774037
$BeO \rightarrow Be + \frac{1}{2}O_2$	$Be + CH_3COOH \rightarrow BeO + CH_3CHO$	608.354	452.7674	-329.833	0.150072
$\frac{1}{3}Y_2O_3 \rightarrow \frac{2}{3}Y + \frac{1}{2}O_2$	$\frac{2}{3}Y + CH_3COOH \rightarrow \frac{1}{3}Y_2O_3 + CH_3CHO$	635.1033	491.878	-366.04	0.986999
$\frac{1}{3}In_2O_3 \rightarrow \frac{2}{3}In + \frac{1}{2}O_2$	$\frac{2}{3}In + CH_3COOH \rightarrow \frac{1}{3}In_2O_3 + CH_3CHO$	308.5963	150.5445	-36.1553	1.274687
$\frac{1}{3}Sc_2O_3 \rightarrow \frac{2}{3}Sc + \frac{1}{2}O_2$	$\frac{2}{3}Sc + CH_3COOH \rightarrow \frac{1}{3}Sc_2O_3 + CH_3CHO$	636.2733	488.7037	-365.873	0.499084
$ThO_2 \rightarrow ThO + \frac{1}{2}O_2$	$ThO + CH_3COOH \rightarrow ThO_2 + CH_3CHO$	1201.31	807.9806	-840.997	4.130431
$ThO \rightarrow Th + \frac{1}{2}O_2$	$Th + CH_3COOH \rightarrow ThO + CH_3CHO$	25.104	139.4778	149.8541	3.863992
$\frac{1}{2}ThO_2 \rightarrow \frac{1}{2}Th + \frac{1}{2}O_2$	$\frac{1}{2}Th + CH_3COOH \rightarrow \frac{1}{2}ThO_2 + CH_3CHO$	613.207	473.7292	-345.571	1.931996
$\frac{1}{2}UO_2 \rightarrow \frac{1}{2}U + \frac{1}{2}O_2$	$\frac{1}{2}U + CH_3COOH \rightarrow \frac{1}{2}UO_2 + CH_3CHO$	542.4495	414.0214	-278.654	1.981878
$Cu_2O \rightarrow 2Cu + \frac{1}{2}O_2$	$2Cu + CH_3COOH \rightarrow Cu_2O + CH_3CHO$	170.707	59.96508	87.22384	2.116388
$\frac{1}{2}PtO_2 \rightarrow \frac{1}{2}Pt + \frac{1}{2}O_2$	$\frac{1}{2}Pt + CH_3COOH \rightarrow \frac{1}{2}PtO_2 + CH_3CHO$	-85.3535	-82.0273	301.9969	1.624276
$\frac{1}{2}ReO_2 \rightarrow \frac{1}{2}Re + \frac{1}{2}O_2$	$\frac{1}{2}Re + CH_3COOH \rightarrow \frac{1}{2}ReO_2 + CH_3CHO$	224.4715	174.1381	47.94445	1.550398
$RuO_4 \rightarrow RuO_3 + \frac{1}{2}O_2$	$RuO_3 + CH_3COOH \rightarrow RuO_4 + CH_3CHO$	105.855	-20.2631	157.6866	2.482341
$\frac{1}{2}RuO_2 \rightarrow \frac{1}{2}Ru + \frac{1}{2}O_2$	$\frac{1}{2}Ru + CH_3COOH \rightarrow \frac{1}{2}RuO_2 + CH_3CHO$	152.507	56.73922	110.4409	0.84153
$\frac{1}{2}OsO_4 \rightarrow \frac{1}{2}OsO_2 + \frac{1}{2}O_2$	$\frac{1}{2}OsO_2 + CH_3COOH \rightarrow \frac{1}{2}OsO_4 + CH_3CHO$	21.1145	89.80119	190.0686	1.850074
$\frac{1}{2}OsO_2 \rightarrow \frac{1}{2}Os + \frac{1}{2}O_2$	$\frac{1}{2}Os + CH_3COOH \rightarrow \frac{1}{2}OsO_2 + CH_3CHO$	147.486	29.35076	118.6875	1.583644
$SiO_2 \rightarrow SiO + \frac{1}{2}O_2$	$SiO + CH_3COOH \rightarrow SiO_2 + CH_3CHO$	810.441	416.3205	-454.742	0.734122
$SiO \rightarrow Si + \frac{1}{2}O_2$	$Si + CH_3COOH \rightarrow SiO + CH_3CHO$	100.416	227.6054	74.59653	0.467683
$\frac{1}{2}SiO_2 \rightarrow \frac{1}{2}Si + \frac{1}{2}O_2$	$\frac{1}{2}Si + CH_3COOH \rightarrow \frac{1}{2}SiO_2 + CH_3CHO$	455.4285	321.963	-190.073	0.233841
$\frac{1}{3}Sb_2O_3 \rightarrow \frac{2}{3}Sb + \frac{1}{2}O_2$	$\frac{2}{3}Sb + CH_3COOH \rightarrow \frac{1}{3}Sb_2O_3 + CH_3CHO$	240.1017	121.0933	25.19465	1.351621
$\frac{1}{3}Bi_2O_3 \rightarrow \frac{2}{3}Bi + \frac{1}{2}O_2$	$\frac{2}{3}Bi + CH_3COOH \rightarrow \frac{1}{3}Bi_2O_3 + CH_3CHO$	191.294	68.38608	74.07074	2.320014

Appendix D: Experimental yields

In addition to the values for selectivity to organic products presented in Section 4.2 of the main text, we present herein the yield of each product, as measured in the experimental setup described in Section 4.1 of the main text. Figures 5 and 6 below give the carbon-weighted yields of each reaction product in the ZnO HDO and Zn LOC experiments, as well as the total yield summed over all products. The carbon-weighted yield is defined as:

$$\text{Yield}_i(\%) = \frac{p_i C_i}{2p_{\text{AcOH}}} \tag{12}$$

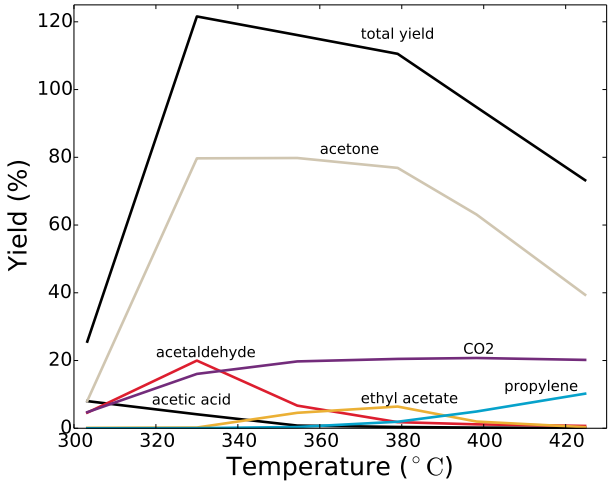

Figure 5: Carbon-weighted yield (see Equation 12) of all products of ZnO-catalyzed HDO plotted as a function of temperature.

As in Equation 7, p_i and C_i denote the partial pressure and number of carbon atoms in product i,

respectively. p_{AcOH} denotes the partial pressure of acetic acid in the feed stream to the upgrading reactor and the number 2 in the denominator derives from the number of carbon atoms in acetic acid. Notably, the total yield in Figure 5 is not consistently 100%, indicating that a carbon-balance on the reactor is not closed. This could be explained by the carbon deposition and subsequent decomposition and desorption at the metal oxide surface. Figure 6 illustrates that the carbon-balance is closed for the LOC deoxygenation of acetic acid to acetaldehyde at 350°C, as the total yield remains close to 100% and stabilizes after the reaction has proceeded for 100 minutes.

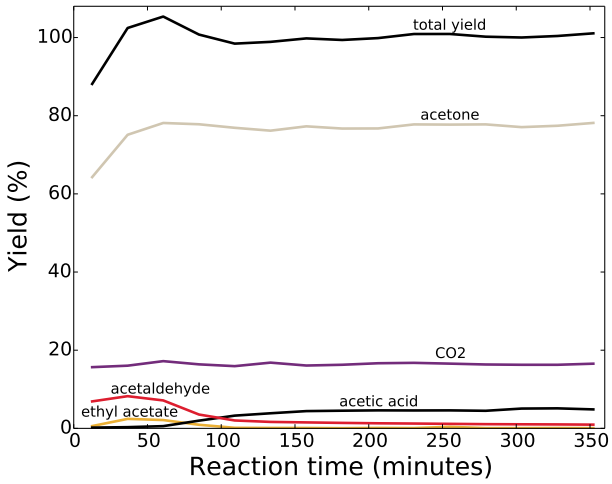

Figure 6: Carbon-weighted yield of all LOC products plotted as a function of reaction time.

References

[1] Ewan, B.; Allen, R. Limiting thermodynamic efficiencies of thermochemical cycles used for hydrogen generation. *Green Chem.* **2006**; , 988–994.

[2] Fletcher, E.a.; Moen, R.L. Hydrogen and oxygen from water. *Science* **1977**; 197, 1050–6.

[3] Steinfeld, A. Solar hydrogen production via a two-step water-splitting thermochemical cycle based on Zn/ZnO redox reactions. *Int. J. Hydrogen Energy* **2002**; 27, 611–619.

[4] Steinfeld, A.; Palumbo, R. Solar thermochemical process technology. *Encycl. Phys. Sci. Technol.* **2001**; 15, 237–256.

[5] Kodama, T.; Gokon, N. Thermochemical cycles for high-temperature solar hydrogen production. *Chem. Rev.* **2007**; 107, 4048–77.

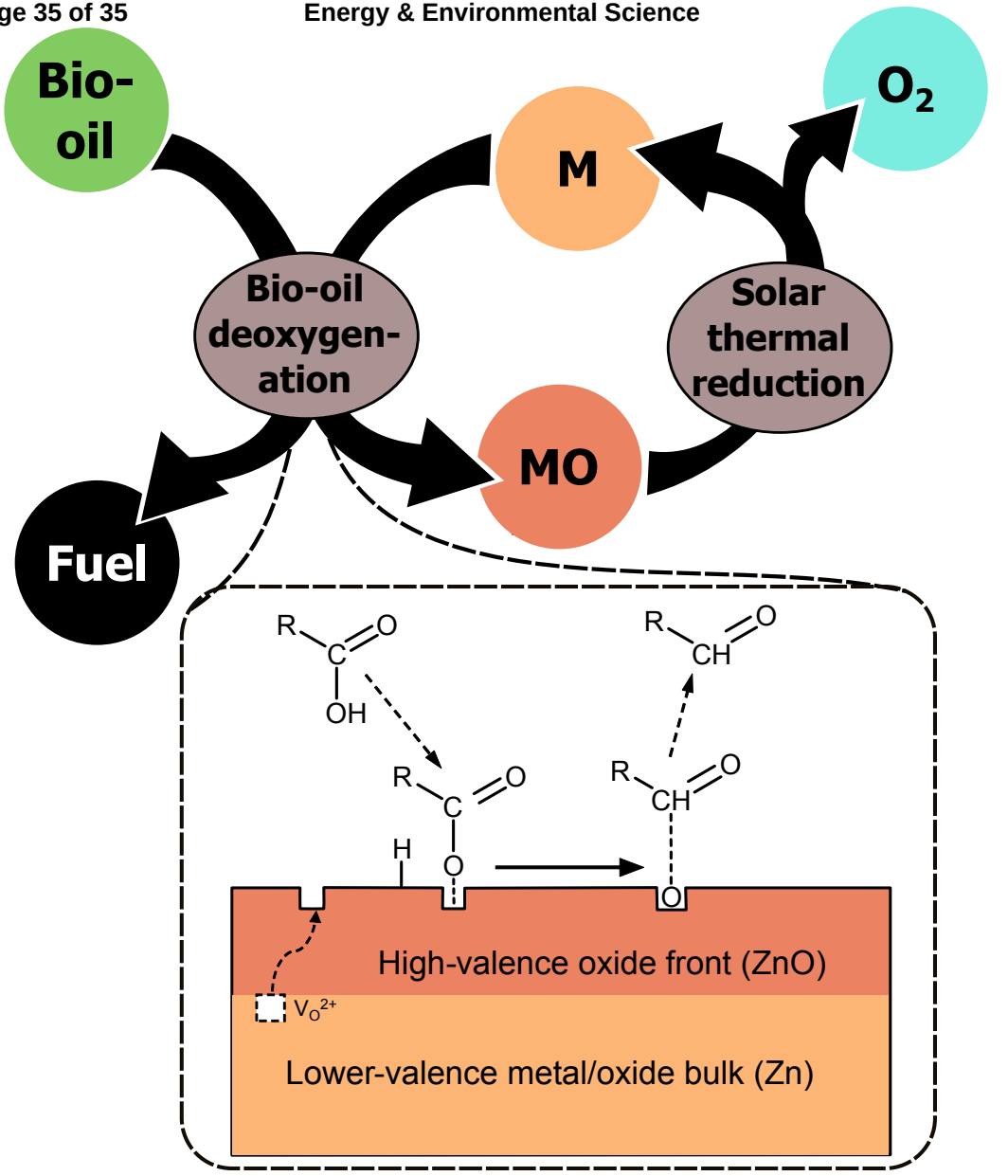
Bio-oil
M
O_2
Bio-oil deoxygen-ation
Solar thermal reduction
MO
Fuel
R
C
O
OH
H
CH
High-valence oxide front (ZnO)
V_O^{2+}
Lower-valence metal/oxide bulk (Zn)